Author Manuscript

Title: Building Blocks for High-Efficiency Organic Photovoltaics. Interplay of Molecular, Crystal, and Electronic Properties of Post-Fullerene ITIC Ensembles

Authors: Steven M. Swick; Tim Gebraad; Leighton Jones; Bo Fu; Thomas J. Aldrich; Kevin L. Kohlstedt; George C. Schatz; Antonio Facchetti; Tobin Jay Marks

To be cited as: ChemPhysChem 10.1002/cphc.201900793

Link to VoR: https://doi.org/10.1002/cphc.201900793

Building Blocks for High-Efficiency Organic Photovoltaics. Interplay of Molecular, Crystal, and Electronic Properties in Post-Fullerene ITIC Ensembles

Steven M. Swick[a,1,2], Tim Gebraad[a,1,2], Leighton Jones[1,2], Bo Fu[1,2], Thomas J. Aldrich[1,2], Kevin L. Kohlstedt*[,1,2,], George C. Schatz*[,1,2], Antonio Facchetti*[,1,2], Tobin J. Marks*[,1,2]

[1]Department of Chemistry, Northwestern University, Evanston, Illinois 60208, United States

[2]Center for Light Energy Activated Redox Processes, Evanston, Illinois 60208, United States

[a] These authors contributed equally.

*To whom correspondence may be addressed. Email: K.L.K. (kkohlstedt@northwestern.edu, (847) 491-2951), G.C.S. (g-schatz@northwestern.edu, (847) 491-5657), A.F. (a-facchetti@northwestern.edu, (847) 491-3307), and T.J.M. (t-marks@northwestern.edu, (847) 491-5658)

Abstract: Accurate single-crystal x-ray diffraction data offer a unique opportunity to compare and contrast the atomistic details of bulk heterojunction photovoltaic small-molecule acceptor structure and packing, as well as provide an essential starting point for computational electronic structure and charge transport analysis. Here we report diffraction-derived crystal structures and computational analyses on the n-type semiconductors which enable some of the highest efficiency organic solar cells produced to date, 3,9-bis(2-methylene-(3-(1,1-dicyanomethylene)-indanone))-5,5,11,11-tetrakis(4-hexylphenyl)-dithieno[2,3-*d*:2',3'-*d*']-s-indaceno[1,2-*b*:5,6-*b*']dithiophene (**ITIC**) and seven derivatives (including three new crystal structures: 3,9-bis(2-methylene-(3-(1,1-dicyanomethylene)-indanone))-5,5,11,11-tetrakis(4-propylphenyl)-dithieno[2,3-*d*:2',3'-*d*']-s-indaceno[1,2-*b*:5,6-*b*']dithiophene (**ITIC-C3**), 3,9-bis(2-methylene-(3-(1,1-dicyanomethylene)-indanone))-5,5,11,11-tetrakis(3-hexylphenyl)-dithieno[2,3-*d*:2',3'-*d*']-s-indaceno[1,2-*b*:5,6-*b*']dithiophene (***m*-ITIC-C6**), and 3,9-bis(2-methylene-((3-(1,1-dicyanomethylene)-6,7-difluoro)-indanone))-5,5,11,11-tetrakis(4-butylphenyl)-dithieno[2,3-*d*:2',3'-*d*']-s-indaceno[1,2-*b*:5,6-*b*']dithiophene (**ITIC-C4-4F**). IDTT acceptors typically pack in a face-to-face fashion with π-π distances ranging from 3.28-3.95 Å. Additionally, edge-to-face packing is observed with S···π interactions as short as 3.21-3.24 Å. Moreover, **ITIC** end group identities and side chain substituents influence the nature and strength of noncovalent interactions (e.g. H-bonding, π-π) and thus correlate with the observed packing motif, electronic structure, and charge transport properties of the crystals. Density functional theory (DFT) calculations reveal relatively large nearest-neighbor intermolecular π-π electronic couplings (5.85-56.8 meV) and correlate the nature of the band structure with the dispersion interactions in the single crystals and core-end group polarization effects. Overall, this combined experimental and theoretical work reveals key insights into crystal engineering strategies for indacenodithienothiophene (IDTT) acceptors, as well as general design rules for high-efficiency post-fullerene small molecule acceptors.

Introduction

As the need to develop new and commercially viable green energy technologies becomes increasingly urgent, organic solar cells (OSCs) have attracted great interest due to their amenability to solution processing, scalability, low cost, low toxicity, mechanical flexibility and light weight.[1] Bulk heterojunction (BHJ) OSCs, which function *via* the exciton splitting and charge transporting capabilities of a phase-separated contiguous hole conducting network (typically a polymer) blended with a phase-separated contiguous electron conducting network (typically a small molecule), have seen rapid advances in photovoltaic metrics. Thus, power conversion efficiency (PCE) in the last few years has increased beyond 15%.[2] These rapid advances in PCE have largely relied on the development of new non-fullerene acceptors (NFAs),[3] with Zhan's original report of 3,9-bis(2-methylene-(3-(1,1-dicyanomethylene)-indanone))-5,5,11,11-tetrakis(4-hexylphenyl)-dithieno[2,3-*d*:2',3'-*d*']-s-indaceno[1,2-*b*:5,6-*b*']dithiophene (**ITIC**, Figure 1)[4] heralding the post-fullerene era for OSCs.

The remarkable NFA-driven PCE advances reflect superior bulk-heterojunction (BHJ) morphologies, large NFA oscillator strengths in important regions of the solar spectrum, and synthetic tunability enabling the rapid synthesis and evaluation of many novel NFA structures. Nevertheless, how planar indacenodithienothiophene (IDTT, **Figure 1**) acceptors such as **ITIC** can match or exceed the remarkable charge transporting and exciton splitting efficiencies of spherically shaped, isotropically charge transporting fullerenes has remained enigmatic. Specifically, while the packing arrangements that would give rise to continuous fullerene networks seems obvious, the case for IDTT molecules remains a mystery. Furthermore, thin-film characterization techniques such as transmission electron microscopy, atomic force microscopy, resonant soft x-ray scattering, grazing incidence wide angle x-ray scattering (GIWAXS), femtosecond transient absorption spectroscopy, space-charge limited current measurements and others have provided a wealth of data on NFA nanoscale/mesoscale organization, photophysical/charge transport properties, and how these properties correlate with OSC performance.[5] Nevertheless, these techniques do not provide atomistic details of NFA molecular geometries, nor how assemblies of these molecules pack and transport charge. In addition, purely

computationally approaches to understanding bulk charge transport in NFA OSCs must rely on coarse approximations of the BHJ morphology, such as mean-field and coarse-grained approaches.[6]

Single crystal x-ray diffraction (XRD) structural information addresses these issues in that it provides atomistic details of small molecule geometry and packing and serves as a BHJ-relevant starting point for computations. Indeed, these results are now being used for rational NFA design[7] and for computational evaluation of their charge transport properties.[8] Note that although some BHJs may contain amorphous acceptor and donor domains, this does not diminish the importance of single crystal XRD for the study of NFA-based blends because, 1) many high-performing NFAs form extensive crystalline domains within BHJ active layers,[2, 8b, 9] and 2) acceptor periodicity parameters measured by thin film x-ray techniques (such as GIWAXS) have been found to be consistent with those simulated from single crystal x-ray structures, thus confirming the presence of crystalline regions in the BHJ with molecular packing similar to that in the single crystal structure.[7c-e, 8b, 9g, 10]

Computational efforts that rely on thermodynamics for morphological predictions are particularly well-suited for studying minimum energy structures such as those in NFA crystals.[11] While NFA crystallization may depend on processing conditions (e.g., solvent, additives) and donor polymer architecture, perturbations of crystalline domains at an energetic minimum in a blend film can be more easily compared with structural measurements such as x-ray and electron diffraction data.[11b, 12] Conversely, mean-field approaches such as the use of phenomenological free-energy functionals to predict the miscibility of two phases are better suited towards molecules that have little internal structural order due to enthalpic interactions being averaged.[6c, 13]

Structure-property relationships can be more directly determined when the molecular structure and molecular packing are more accurately known. Optoelectronic material properties such as electronic coupling, valence and conduction band density of states, hole and electron carrier mobilities, and exciton separation are all intimately tied to the intermolecular structure of the crystal. Elucidation of the relationships between NFA topology and properties of the crystals will be key to developing rational design strategies to further fine tune BHJ morphological details for enhanced OSC performance.

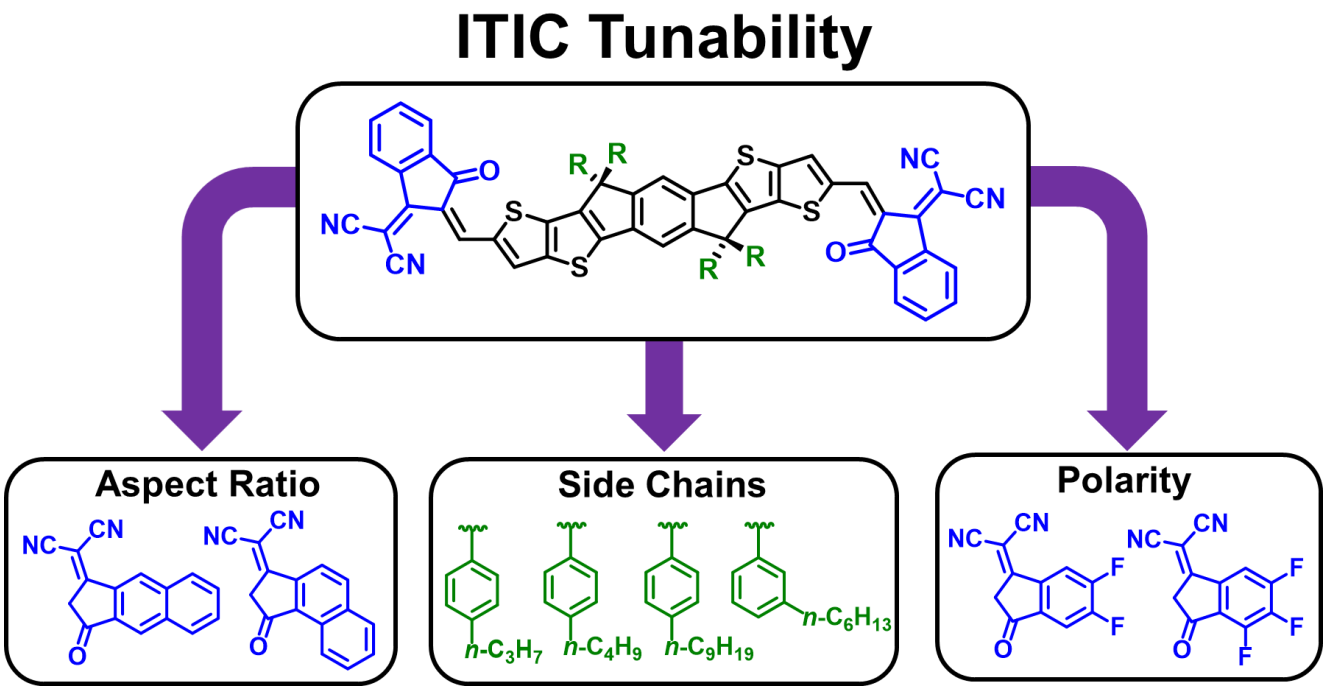

Figure 1. Chemical design space of IDTT derivatives of **ITIC**. Aspect ratio of end groups leads to greater acceptor π-π electronic overlap. End group functionalization with polar groups such as fluorine atoms leads to increased **ITIC** polarity and greater dispersion interactions between neighboring molecules in the crystal. Side chain engineering allows control of crystallite dimensions and π-π-stacking distances.

Computational Analysis of Crystal Structure-Transport Relationships

As small molecule acceptors, most notably fullerenes, became the champion materials in BHJ solar cells, there was a focus to understand the relationship between molecular organization and cell performance.[13-14] Computational methods provided a vital connection to predict the influence of molecular organization on charge generation and transport.[14a, 14b, 15] Indeed, before these structure-property relationships could be established, an

understanding of the thermodynamics of molecular packing was necessary to describe both the energetic driving forces for molecular organization[14c, 16] and the effect of thermal disorder.[11a, 17] Here statistical thermodynamic methods have been key in modeling the energetics of the molecular packing-both crystalline and amorphous.[11a, 18] In particular, molecular dynamics and Monte Carlo sampling methods can provide the organic semiconductor community a fundamental and microscopic view of the driving forces behind OSC morphology. This is especially true with small molecules, where kinetically trapped structures are less likely than with conjugated polymers. In the absence of crystal structure data, the only recourse is to use a DFT level of theory to generate a potential energy surface (PES) between pairs of molecules and attempt to map out minimum energy geometries.

Fullerenes and fullerene derivative structures have been intensely studied over the last decade to understand why they so successfully function as the "AB blood type" equivalent n-type universal electron acceptor, which led to an ultrafast charge separation model due to the spatial delocalization of the orbitals.[19] Computational efforts focused on degenerate conduction band energy levels in fullerenes[20] and charge percolation pathways in fullerene crystals[11c, 21] as properties promoting proficiency in exciton separation and high electron mobility. In particular, electronic structure studies concentrated on calculating (LUMO-LUMO) electronic couplings (J) between neighboring sites in fullerene crystals.[22] J values could then be used to predict lifetimes in charge hopping kinetics and subsequently predict electron mobility[23], or J could be used in tight-binding Hamiltonians that model the excited state dynamics and test the underlying transport mechanisms.[24]

In organic crystalline environments, especially when there is appreciable electronic overlap as in fullerenes, it is important to recognize that the molecular eigenstates will hybridize and states will mix (broaden). Calculating or measuring the density of states (DOS) has been useful to understand the available states that can be used in charge transport.[25] Additionally, the DOS can be useful to determine which atomic orbitals comprise the molecular eigenstates within the crystals.[8b] This is especially useful when there are different functional groups within the acceptor molecule, such as in the **ITIC** class of acceptors. From the DOS, the band structure can be calculated by projecting the available states along different crystal directions. The band structure allows one to see how degenerate the states are through the Bravais lattice (k-space) of the crystal.[26] For bands with low k-space degeneracy, transport carriers behave more freely due to their effective mass being smaller *e.g*. a parabolic energy *vs* k-space scaling. The energy calculations for DOS plots are often computed at DFT level of theory that includes a dispersion correction term to account for the delocalized π-electrons.[27]

If one could collect and classify a set of crystal structures, such calculations would provide an informative means to compare their charge transport properties and relate them to the crystal structural details. In the case of the **ITIC**-based structures, many of the crystals are qualitatively similar π-stacked motifs, requiring closer inspection and detailed computation. To differentiate the structures, J values are compared across the different structures along different crystal directions, DOS plots are computed near the band edges allowing bandwidths and available transport states to be compared, and a PES was computed in detail for a **ITIC** variant.

In this contribution we compare and contrast the single crystal diffraction-derived crystal structures and computational analysis of 8 NFAs containing the IDTT core because 1) IDTT molecules comprise a rich class of single crystal structures (**Figure 2**), 2) they are among the most widely employed class of NFAs,[3a, 3d, 3f] and 3) many high-PCE OSC active layers contain IDTT acceptors,[3a, 3d, 3f] and are thus relevant to the design of next-generation organic photovoltaics. We begin with crystallographic and computational analysis of each individual molecule, including the previously unreported crystal structures of **ITIC-C3**, ***m*-ITIC-C6**, and **ITIC-C4-F4**, followed by a discussion correlating the effects of IDTT side chain length and substitution position, end group polarity, and end group aspect ratio on single molecule conformation, crystal structure packing, electronic structure, and charge transport with an emphasis on computational analysis-structure-transport correlations. In addition, we analyze the crystal structure packing motifs and the intra/inter-molecular forces that underlie these unique patterns of molecular organization and interpret them in the context of fullerenes and perylene diimide acceptors in order to derive rational design rules for small molecule acceptors. Full details of the different methods used for the computational analysis are available in the Supporting Information.

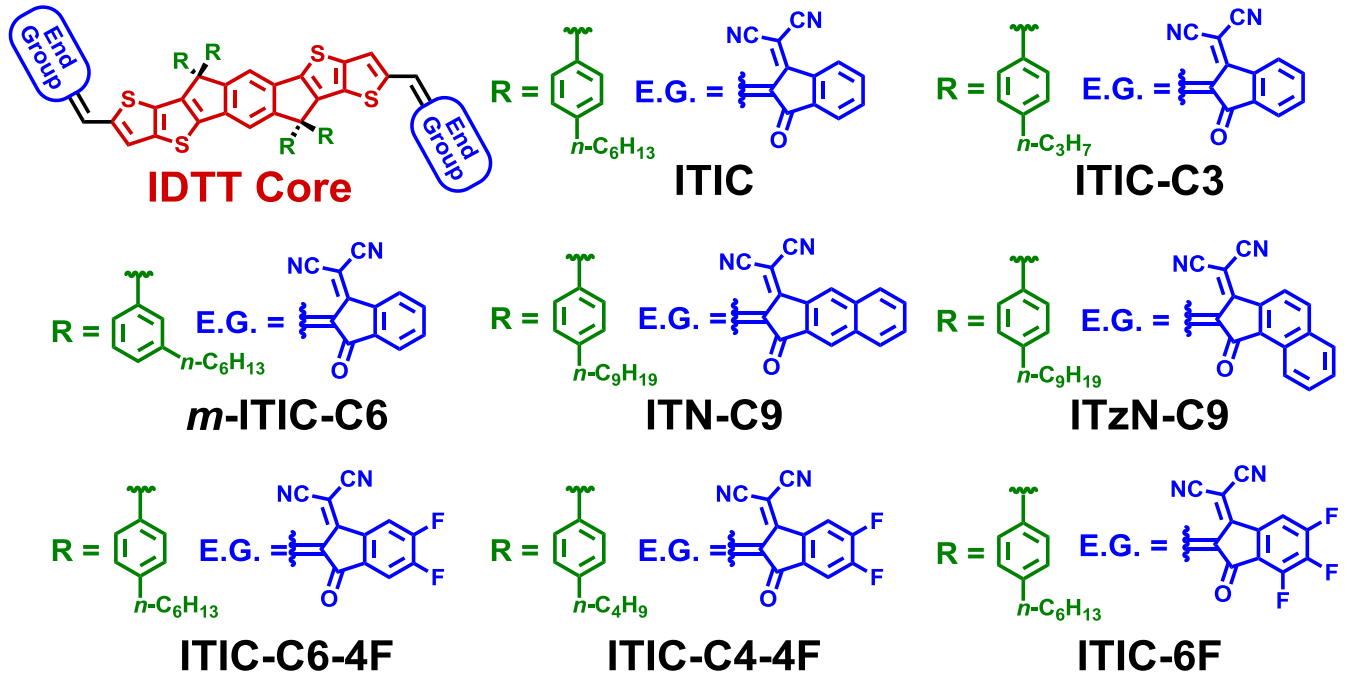

Figure 2. Molecular structures of the IDTT acceptors discussed in this study.

Results

IDTT NFA crystal structures

Crystal Growth. In order to obtain optimal morphologies in BHJ active layers (i.e., those facilitating efficient exciton generation, separation, and charge transport), high-efficiency IDTT NFAs must be designed so that in the blend film they do not form crystalline domains of dimensions exceeding the nanoscale. For this reason, the experimental task of growing diffraction-quality crystals can be challenging, as some crystals nucleate with difficulty and tend to be small and/or grow in clusters. Solvent vapor diffusion is often the most effective method to grow diffraction quality crystals. Interestingly, the unconventional solvent dibromomethane (CH_2Br_2) is particularly effective in producing high quality crystals, likely because the low volatility (b.p. = 96-98 °C) permits the use of low volatility counter solvents, slowing the crystallization process. Interestingly, CH_2Br_2 was also found to incorporate into the crystal structures of about half of the IDTT acceptors reported here (**ITIC** polymorph 1, **ITIC-C3**, ***m*-ITIC-C6**, **ITN-C9**, and **ITzN-C9**). The CH_2Br_2 molecules fill voids between side chains, and in some cases are found to occupy large core-core voids that are typical of face-to-face packed molecules.

Single Molecule Conformation and Crystal Packing. IDTT acceptors generally exhibit planar conformations that are enforced by intramolecular S···O interactions[28] between the IDTT core and the end groups (**Figure 3A**). Torsions between the end group and the IDTT core were calculated using the planes defined by atoms 1-4 (labeled for clarity). Within the IDTT core are two tetrahedral (sp^3) carbons where the alkyl phenyl substituents are attached, creating steric bulk above and below the molecular plane. In addition to imbuing the NFA with solubility, tuning energy levels,[29] and modulating crystallinity and aggregation,[9f, 30] these alkyl phenyl substituents play the critical role in limiting π-π interactions between molecules. This typically results in a face-to-face, slip-stacked packing motif that is driven by interactions between the end groups (**Figure 3B**), although edge-to-face type packing exists as well (**Figure 3C**). This sheds light on the sensitivity of the morphology of IDTT acceptor films with regard to small changes in the end group structure.[8b, 31]

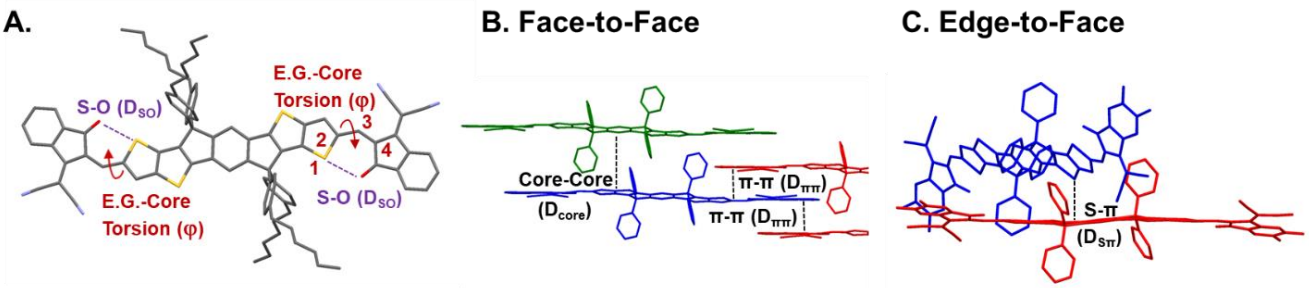

Figure 3. Schematic representation of **A.** IDTT core conformation, where E.G. = end group **B.** IDTT slip-stacked, face-to-face packing motif, and **C.** IDTT edge-to-face packing motif.

For simplicity, the following abbreviations and definitions will be used: S···O distance (D_{SO}, **Figure 3A**), end group-core torsions (φ, **Figure 3A**), π-π distances ($D_{ππ}$, **Figure 3B**), S···π distances ($D_{Sπ}$, **Figure 3C**), centroid-centroid distances (D_{cent}): distance between the centroids of two π-π interacting molecules in face-to-face packing or the distance between the centroids of two S···π interacting molecules in edge-to-face packing, and core-core distances (D_{core}): distance between the planes defined by the cores of two molecules which roughly eclipse each other when viewed along the π-stacking direction in the face-to-face motif.

Table 1. Summary of IDTT Acceptor Crystal Structure Properties.

Acceptor	Solvent System	Packing Motif	D_{SO} (Å)	φ (°)	D_{Cent} (Å) [a]	Greatest |J| Value (meV)	E_{disp} (kcal/cm^3) [b]
ITIC-Poly1	CH_2Br_2: *n*-heptane	Face-to-Face	2.66 2.80	4.1 0.4	19.42, 23.99	11.4	-139
ITIC-Poly2	CH_2Cl_2: Pet. Ether	Edge-to-Face	2.72 2.75	9.3 13.4	7.73	16.0	-
ITIC-C3	CH_2Br_2: *n*-heptane	Face-to-Face	2.71 2.71	1.9 3.8	19.27, 23.32	-	-1535
***m*-ITIC-C6**	CH_2Br_2: *n*-heptane	Face-to-Face	2.67 2.70	5.3 1.4	17.34, 22.37	19.22	-613
ITN-C9	CH_2Br_2: acetone	Face-to-Face	2.79	3.7	21.68, 26.32	5.9	-
ITzN-C9	CH_2Br_2: acetone	Face-to-Face	2.62 2.75	7.4 1.9	19.81, 23.94	38.8	-
ITIC-C6-4F	CH_2Br_2: *n*-heptane	Hybrid	2.71 2.82	10.1 7.9	7.71,[c] 21.56 [d]	17.1	-135
ITIC-C4-4F	CH_2Br_2: *n*-heptane	Face-to-Face	2.70	0.6	15.92	-	-197
ITIC-6F	CH_2Br_2: *n*-heptane	Face-to-Face	2.70	0.8	15.83, 19.94	56.8	-174

[a] Centroid-centroid distances between π-π interacting neighbors for face-to-face packed molecules, or between S···π interacting neighbors for edge-to-face packed molecules.
[b] Dispersion energy density
[c] S···π interacting centroid-centroid distance.
[d] π-π interacting centroid-centroid distance.
[e] dichlorobenzene

Computational Analysis. At first glance, the crystal packing of many IDTT acceptors seems qualitatively similar. Indeed, since the π-face-to-face packing motif is present in nearly all IDTT crystal structures reported here, it can be difficult to distinguish how changes in the chemical structure of the acceptor manifest in the crystal structure and how these changes affect the charge transport properties of a given packing motif. Computation provides quantitative metrics that can be used to analyze and compare the crystal packing between different IDTT acceptors. Computed J values across different crystal symmetries provides a metric that illuminates both the bandwidth and directionality of charge transport. Specifically, by defining a reference molecule in the crystal lattice (usually a molecule at a high-symmetry point) and calculating electronic coupling magnitude |*J*| and phase (±) between the reference and its neighbors, information regarding the charge transporting strength and directionality of a specific interaction can be assessed, respectively. *J* values are calculated through the overlap integral of the frontier molecular orbitals of interest (**Figure 4**). Note that in the case of **ITIC**, the LUMOs are delocalized across the end groups of the molecule, which is expected to facilitate electron transport through π-π overlap of the end groups (*vide infra*).[8b] Depending on the density of states near the bandgap, either HOMO-HOMO or LUMO-LUMO overlaps are calculated for hole and electron transport, respectively; closely lying MOs can be considered as well (*e.g*. HOMO-1…LUMO+1). Here, crystal structures are used to calculate *J* values between an arbitrary reference molecule chosen at a high-symmetry point for each crystal and its neighbors.[32] The MOs are calculated at both the semiempirical level (ZINDO/S) and the DFT level (PBE0). The electronic coupling is calculated using the ZINDO/S wavefunctions for all IDTT crystals except for the ***m*-ITIC-CX** crystal structures, which use DFT. The functional and basis sets utilized for all calculations are summarized in the SI (**Table S2**). The transfer integral calculations for the dimer structures with both ZINDO/S and DFT are also summarized in the SI. *J* values are computed for LUMO-LUMO overlaps unless noted otherwise.

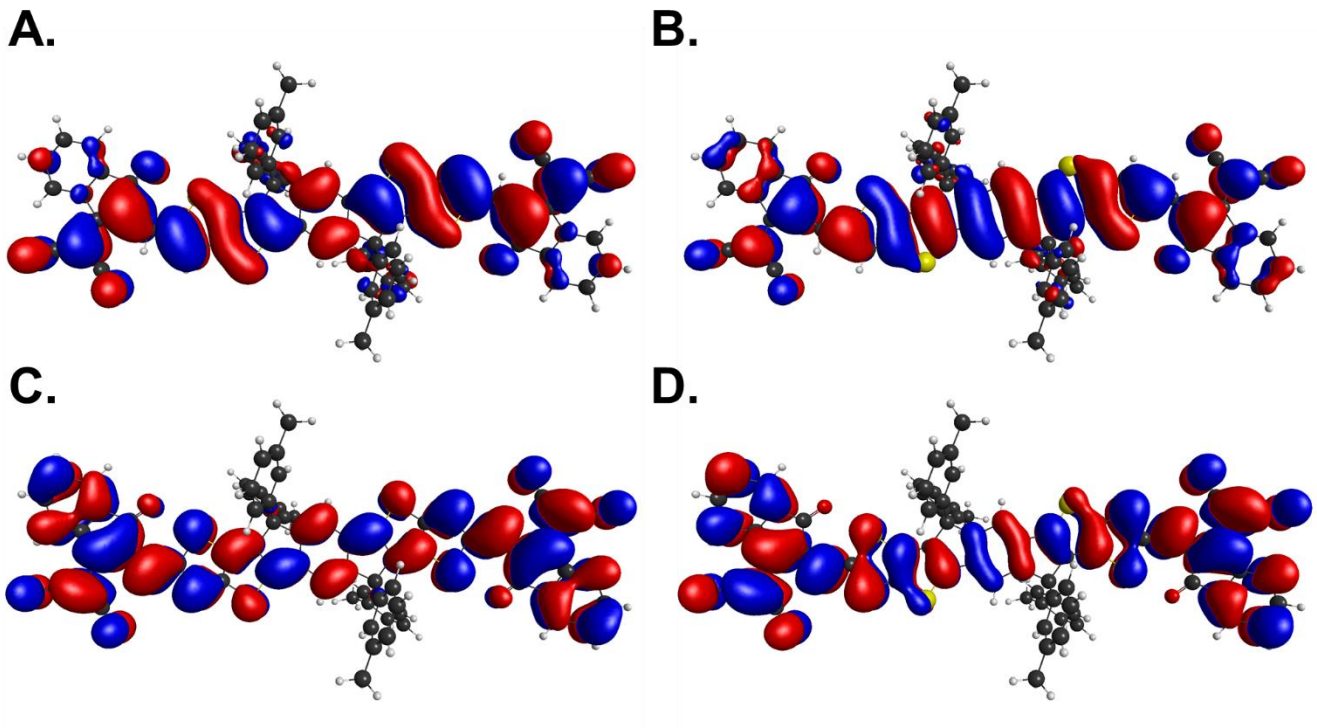

Figure 4. ITIC frontier molecule orbitals (from panel **A** to **D**: HOMO-1, HOMO, LUMO, LUMO+1), obtained from the geometry optimized at the DFT level B3LYP/6-311(d) and a surface isovalue of +/-0.01.

In addition, comparing the density of states (DOS) of the conduction and valence bands for different crystal structures can be insightful for determining the degree of mixing of states and how to relate them to their molecular and crystal structures. Many NFA crystals are in the intermediate coupling limit near 100 meV, where single molecule MOs may be appreciably shifted in the crystal. Additionally, the band structure of the crystal can be calculated from the DOS, which can lead to estimations of the effective mass of the charge carriers. The DOS for different IDTT crystals was calculated using plane-wave (periodic) DFT using a dispersion corrected generalized gradient approximation functional (PBE-D3).

ITIC Crystal Structures

ITIC is known to crystallize in two distinct packing motifs depending on the solvent in which the crystals were grown. When grown from CH_2Br_2/*n*-heptane, **ITIC** packs in a face-to-face slipped stack manner,[8a] whereas crystals grown from CH_2Cl_2/petroleum ether exhibit an edge-to-face[7b] packing motif. This polymorphism underscores the importance of solvent choice for controlling NFA packing, as well as the complexity of NFA solid state packing. Furthermore, this fortuitous discovery of **ITIC** polymorphs indicates that there is more than one energy minimum packing arrangement in the energy landscape of bulk **ITIC**, which is likely the case with other IDTT acceptors as well, due to similarities in their structures. Finally, because of the kinetically controlled nature of BHJ film formation, both of these packing motifs are likely present in BHJ active layers of **ITIC** and other IDTT acceptors (*vide infra*).

ITIC Polymorph 1 Crystal Structure[8a] (Figure 5A)

Single Molecule Conformation and Crystal Packing. Diffraction quality crystals of **ITIC** were grown by slow vapor diffusion of *n*-heptane into a CH_2Br_2 solution. In this polymorph **ITIC** packs in a triclinic lattice and exhibits a planar conformation with D_{SO} = 2.66 Å and 2.80 Å and small corresponding end group to IDTT core torsions (φ = 4.1° and 0.4°), indicating a greater conformationally directed conjugation than polymorph 2 (*vide infra*) and greater HOMO/LUMO delocalization. This also permits more favorable π-π interactions between **ITIC** molecules in polymorph 1, yielding a face-to-face, slip-stacked packing motif with the alkyl phenyl side chains insulating the IDTT cores of the molecules from each other. Within stacks of **ITIC** molecules, short π-π interactions (3.41 Å and 3.35 Å) can be found between the end groups, with corresponding centroid distances of D_{cent} = 23.99 Å and 19.42 Å. The D_{core} between molecules within a stack is >7 Å, indicating that π-π interactions between IDTT cores is negligible.

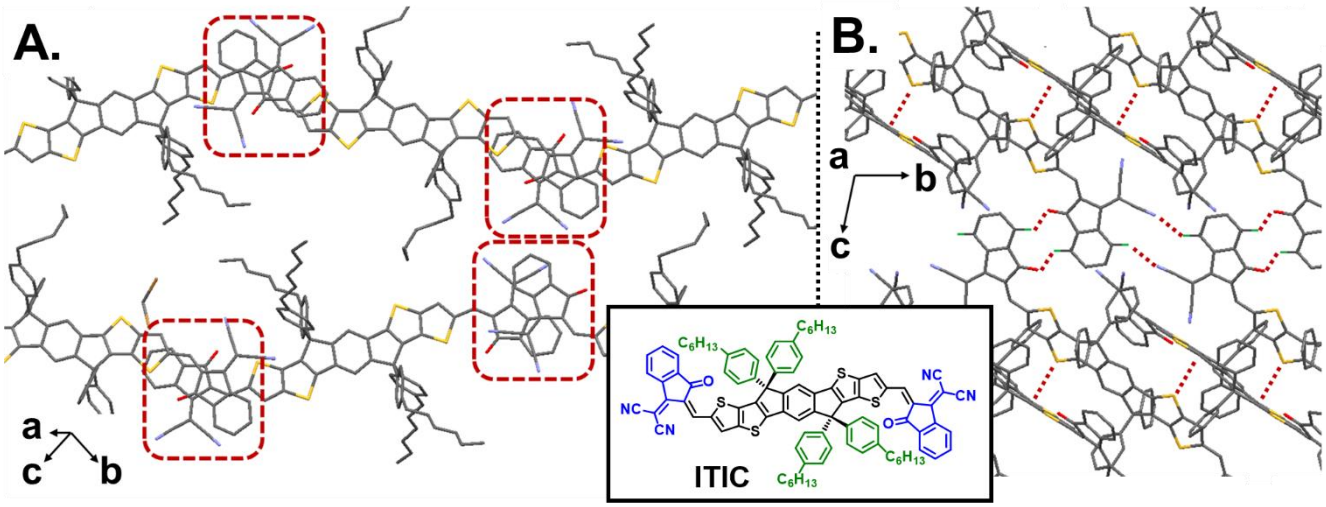

Figure 5. Crystal structure packing diagram of **A. ITIC** polymorph 1 viewed approximately along the *a* crystallographic axis with end group – end group π-π interactions boxed in red, and **B. ITIC** polymorph 2 viewed along the *a* crystallographic axis with S···π and H-bonding interactions shown with red dotted lines, H-bonding hydrogens shown in green, and alkyl chains have been omitted for clarity. In both panels sulfur is yellow, oxygen is red, and nitrogen is blue. The chemical structure of **ITIC** is shown for convenience.

Computational Analysis of Crystal Packing. **ITIC** exhibits modest electronic coupling (*J*) between the reference molecule and its two π-π interacting neighbors (|*J*|=11.4 meV and 3.9 meV). Summing these contributions along the different crystallographic axes, it was found that **ITIC** has a fairly isotropic distribution of |*J*| along the different crystallographic axes, with 30% along the *a* axis, 40% along the *b* axis, and 30% along the *c* axis. The rather isotropic nature of the coupling can be further analyzed by calculating the DOS and band structure of the crystal packing. The band structure and projected DOS of the **ITIC** crystal structure is shown in **Figure 6**. It is immediately evident that the crystal structure has a flat band structure across the symmetry points. Flat band structures are due to degeneracies along different directions of the crystal structure caused by weak orbital overlap for different wavevectors. Comparing to the band structures of subsequent crystal structures it is clear the **ITIC** has relatively weak |*J*| for most crystal orientations, leading to the isotropy. Although the **ITIC** crystal has a degenerate band structure, it does have closely lying conduction band levels that the electron can couple into *e.g.* LUMO+1,…,LUMO+3. Note that closely lying conduction band states have been correlated with higher performing OSCs.[33] The dispersion energy density (E_{disp}) was calculated from a DFT-D3 level electronic structure calculation, which quantifies the amount of van der Waals and H-bonding interactions in the crystal structure. The calculated energy was normalized by the mass and density of the unit cell to make a direct comparison between each crystal. The values are tabulated in **Table 1**.

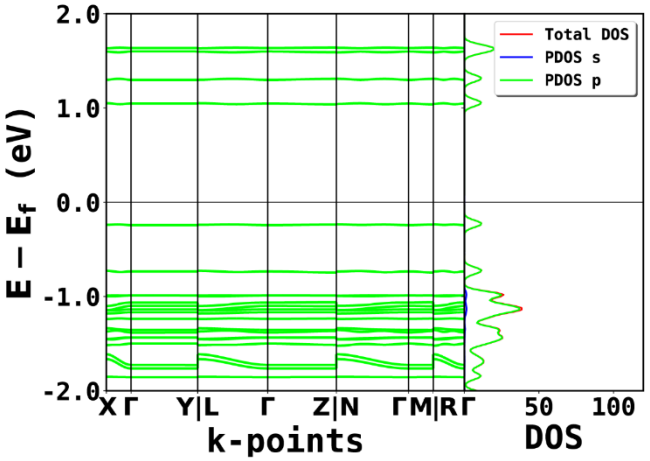

Figure 6. Band structure and DOS of **ITIC** polymorph 1. The Fermi energy (E_f) is defined from the middle of the "HOMO" band. The high-symmetry k-points of the triclinic lattice are plotted from the **Γ**-point (origin) towards the listed lattice directions. The DOS is projected onto s and the three p orbitals with the total DOS being the sum of the four orbitals.

ITIC Polymorph 2 Crystal Structure[7b] **(Figure 5B)**

Single Molecule Conformation and Crystal Packing. Diffraction quality crystals of **ITIC** were grown by slow vapor diffusion of petroleum ether into CH_2Cl_2. In this polymorph **ITIC** packs in a triclinic lattice with D_{SO} = 2.72 Å and 2.75 Å and large end group to IDTT core torsions (φ = 9.3° and 13.4°), consistent with reduced conjugation and greater bond length alternation. Cofacial π-π stacking between **ITIC** molecules is no longer energetically favorable when there is a greater interplanar torsion between the IDTT core and the end groups, and an edge-to-face motif is adopted with $D_{S\pi}$ = 3.24 Å and a D_{cent} = 7.73 Å. Interestingly, the end groups show additional intermolecular H-bonding interactions between end group aryl protons and end group nitrile and carbonyl lone pairs (Ar-H···NΞC and Ar-H···O=C), with interaction distances of 2.62 Å

and 2.47 Å, respectively. These stabilizing interactions provide an additional driving force to pack in an edge-to-face fashion.

Computational Analysis of Crystal Packing. In this single crystal structure, **ITIC** only exhibits electronic coupling between the reference molecule and its edge-to-face interacting neighbors (|J|=16 meV). In addition, this |J| is disposed entirely along the *b* crystallographic axis suggesting that this packing motif can only transport charge in a single dimension. Given the computationally predicted 1D nature of the transport in **ITIC** single crystals it is surprising that relatively high electron mobilities have been calculated for the single crystal (7.4 $\times 10^{-4}$ cm^2 V^{-1} s^{-1}).[7b] Molecular dynamics simulations modeling **ITIC** thin films of non-crystalline **ITIC** have been reported to be even higher (1.46 × 10^{-3} cm^2 V^{-1} s^{-1})[7b] due to higher average couplings arising from end group-end group π-π interactions, highlighting the importance of end groups in facilitating organization of IDTT molecules in the solid state and in charge transport.

ITIC-C3 Crystal Structure (Figure 7)

Single Molecule Conformation and Crystal Packing. Diffraction quality **ITIC-C3** crystals were grown by evaporative diffusion of *n*-heptane into CH_2Br_2 solutions. **ITIC-C3** packs in a monoclinic crystal lattice and exhibits a highly planar conformation with D_{SO} = 2.71 Å and small torsions (φ = 1.9° and 3.8°), lending itself to a face-to-face packing motif with π-π distances between the end groups of 3.39 Å and 3.52 Å and corresponding D_{cent} = 19.27 Å and 23.32 Å. Interestingly however, stacks of **ITIC-C3** are tilted ~45° relative to each other (**Figure 7B**), which is in contrast to other face-to-face packing acceptors of this study where the molecular cores reside in planes that are approximately parallel. Finally, **ITIC-C3** exhibits a large D_{core} (>7 Å).

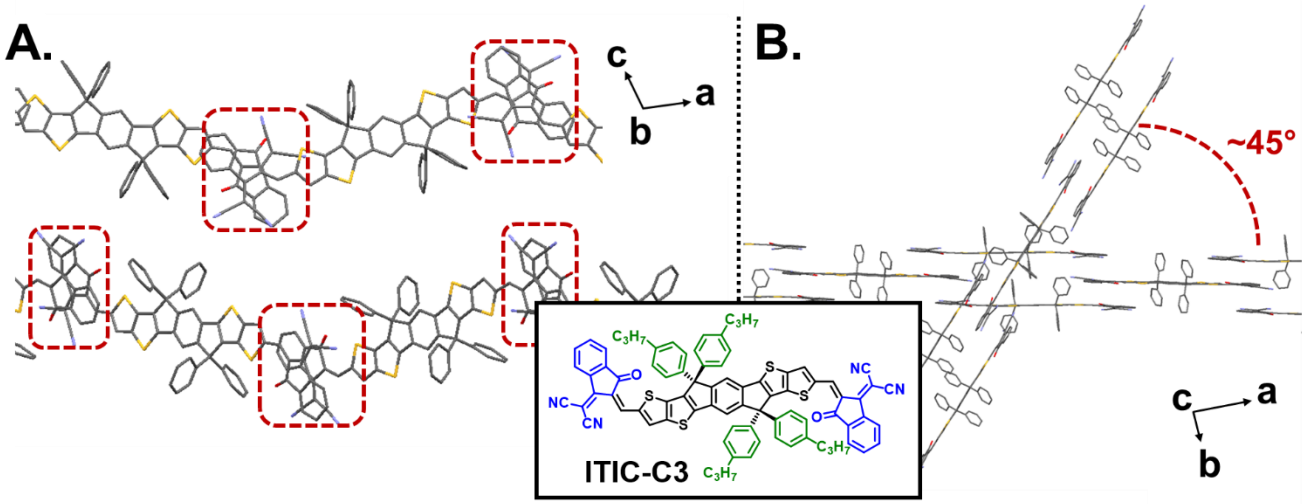

Figure 7. Crystal structure packing diagram of **A. ITIC-C3** viewed along the *b* crystallographic axis with end group – end group π-π interactions boxed in red, and **B. ITIC-C3** viewed along the *c* crystallographic axis. In both panels, alkyl chains have been omitted for clarity, sulfur is yellow, oxygen is red, and nitrogen is blue.

Computational Analysis of Crystal Packing. The planar π-stacks of the **ITIC-C3** structure exhibit a remarkably high π-π dispersion attraction between molecules of the acceptor. To quantify the π-electron dispersion energy, a DFT PBE-level calculation with dispersion corrections was used to calculate the DOS of the crystal. The E_{disp} of the crystal was calculated to be -1535 kcal/cm^3. **ITIC-C3** has been shown to form large domains (>1 μm),[9f] which we attribute to the small side chain length allowing closer face-to-face π-π stacking. By comparison, even with fluorinated end groups, we find that for similar length side chains **ITIC-C4-4F** has E_{disp}=-197 kcal/cm^3. The effect of the side chain length on end group π-stacking was further studied in dimer interactions of ***m*-ITIC-CX** (**Figure 9**, *vide infra*).

***m*-ITIC-C6 Crystal Structure (Figure 8)**

Single Molecule Conformation and Crystal Packing. Diffraction quality ***m*-ITIC-C6** crystals were grown by evaporative diffusion of *n*-heptane into CH_2Br_2 solutions. ***m*-ITIC-C6** packs in a triclinic lattice and exhibits a planar conformation with D_{SO} = 2.67 Å and 2.70 Å and corresponding torsions of φ = 5.3° and 1.4° allowing for a face-to-face packing motif to exist. In addition to π-π interactions between the end groups (π-π distances = 3.36 Å and 3.46 Å, with corresponding D_{cent} = 17.34 Å and 22.37 Å), ***m*-ITIC-C6** also exhibits H-bonding interactions (Ar-H···NΞC) between stacks of acceptors (**Figure 8B, C**), which further stabilize the face-to-face packing motif. The close approach of ***m*-ITIC-C6** molecular columns that enables the H-bonding interactions can be ascribed to the repositioning of the alkyl chains from the *para* to the *meta* position. ***m*-ITIC-C6** also exhibits a large D_{core} spacing of ~6.8 Å.

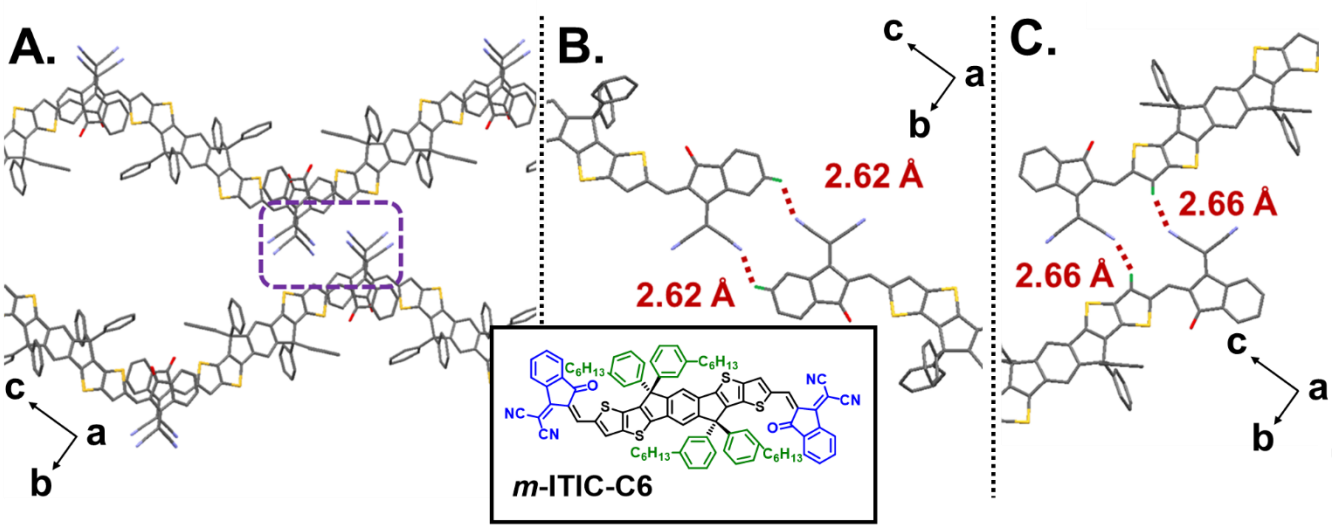

Figure 8. Crystal structure packing diagram of **A. *m*-ITIC-C6** viewed along the *a* crystallographic axis with H-bonding interactions (Ar-H···NΞC) boxed in purple. In panels **B.** and **C.** the H-bonding interactions highlighted in panel **A.** are depicted with red dotted lines. Alkyl chains have been omitted for clarity, sulfur is yellow, oxygen is red, nitrogen is blue, and in panels **B.** and **C.** H-bonding hydrogens are shown in green.

Computational Analysis of Crystal Packing: Computational analysis (DFT; see SI computational methods for details) of ***m*-ITIC-C6** includes a broader analysis than simply the crystal structure. The full potential energy surface (PES) and electronic coupling of a dimer was investigated for a range of side chain lengths (**C1**, **C3**, **C5**, **C6**, and **C7**); see Supporting Information for extended results. **Figure 9** summarizes the PES for both ***m*-ITIC-C1** (**Figure 9B**) and ***m*-ITIC-C6** (**Figure 9C**). Two things are clear from comparing the two PESs. First, the longer side chain of ***m*-ITIC-C6** causes modest disruption of the dimer stack planarity. Second, comparing the π-stacking distance Δz of the four minimum energy geometries between the two side chain lengths, one can see distance is generally greater for the ***m*-ITIC-C6**. Thus, the PESs show how side chains act as "locks" between the energetic minimum and that longer side chains disrupts the cofacial stacking. Of course at some point, the longer side chains will bring the edge-to-face motif into competition with the face-to-face motif. Understanding that competition has not been established to the best of our knowledge.

The DOS of ***m*-ITIC-C6** (**Figure S11**) is similar to that of **ITIC** polymorph 1 and is considered to have fairly isotropic *J*. The *J* values have also been calculated for the entire PES for ***m*-ITIC-C1** (**Figure 10**). Again, two things are of note. First, the dimer geometries have local coupling maxima that correspond to some of the energetic minima (I, III, IV) (see labels in **Figure 9**). Second, the maximum coupling for small amounts of slip (minimum III) approaches 100 meV (94.4 meV). While thermal disorder leads to smaller average J's (**Table 1**), extended end group IDTT acceptors like **ITzN-C9** with larger π-systems or **ITIC** with high degrees of fluorination like **ITIC-6F** show couplings that begin to approach 100 meV. The other sidechain PES studies are shown in the SI (**Figure S2-S6**). From comparing the PESs across the different sidechains it is found that side chain tuning and subsequent crystal engineering offers a viable route to control the degree of slip in the stacked crystals. The amount of slip is critical not only to the amount of coupling, but also the phase, e.g. $J < 0$ J-aggregate and $J > 0$ H-aggregate.[34] As with the **ITIC-C3** structure compared to **ITIC**, altering the side chain position (*meta* vs *para*) allows for greater dispersive interactions leading to a larger E_{disp} = -613 kcal/cm^3 for ***m*-ITIC-C6** compared to E_{disp} = -139 kcal/cm^3 for **ITIC-C6**.

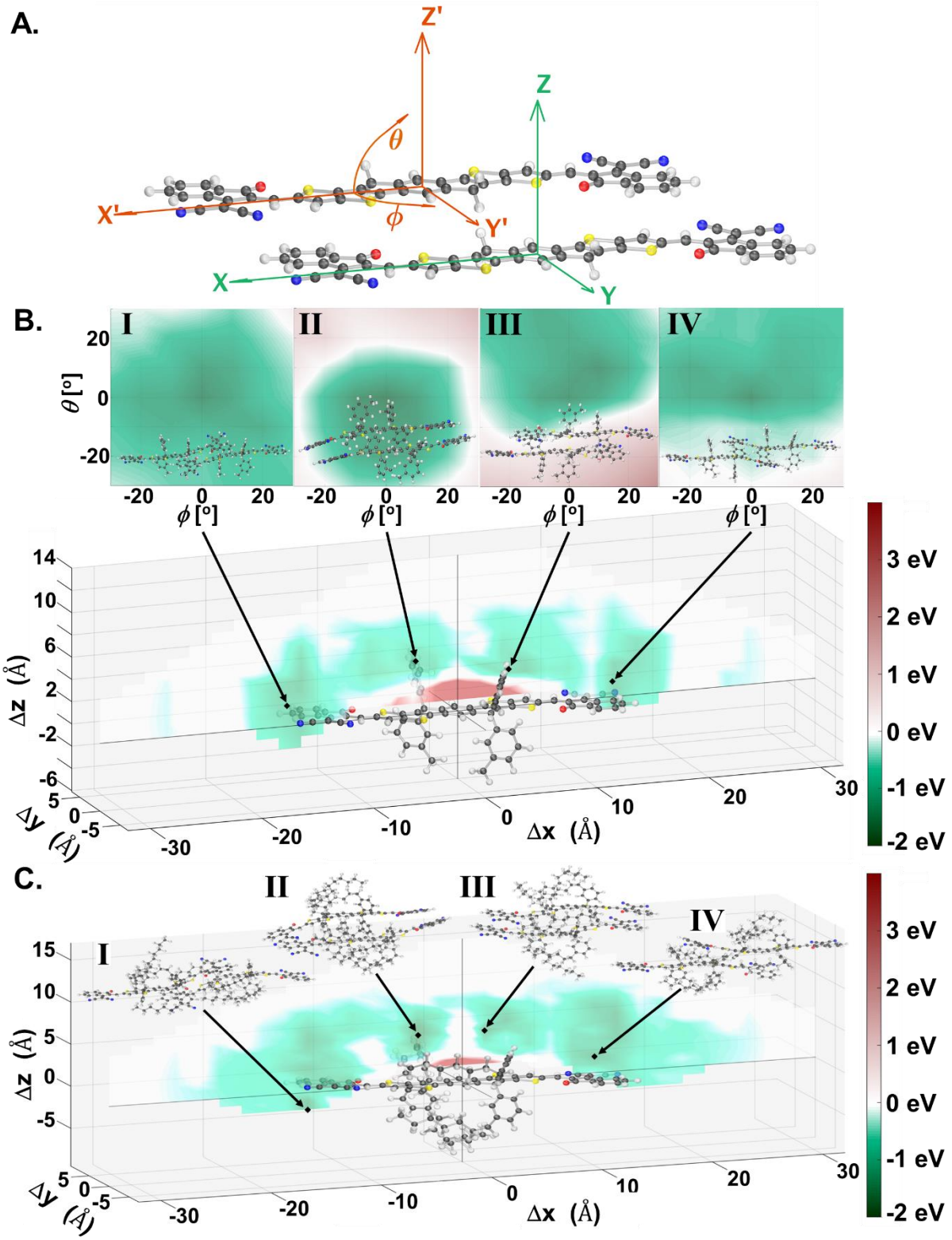

Figure 9. A) ITIC dimer geometric degrees of freedom. Δx, Δy, Δz is defined as X'-X, Y'-Y, Z'-Z, respectively. B) Potential energy surface (PES) of ***m*-ITIC-C1** in xz-plane (slip stack offset vs π-stacking distance). The four minimum energy geometries (I, II, III, IV) are shown in inset boxes along with the PES for the polar rotation θϕ-plane for each geometry. C PES of ***m*-ITIC-C6** with four minimum energy dimer geometries. Note that Δz is measured from IDTT cores and if the dimer shows a large degree of non-planarity then Δz can be smaller than 3 Å or even negative.

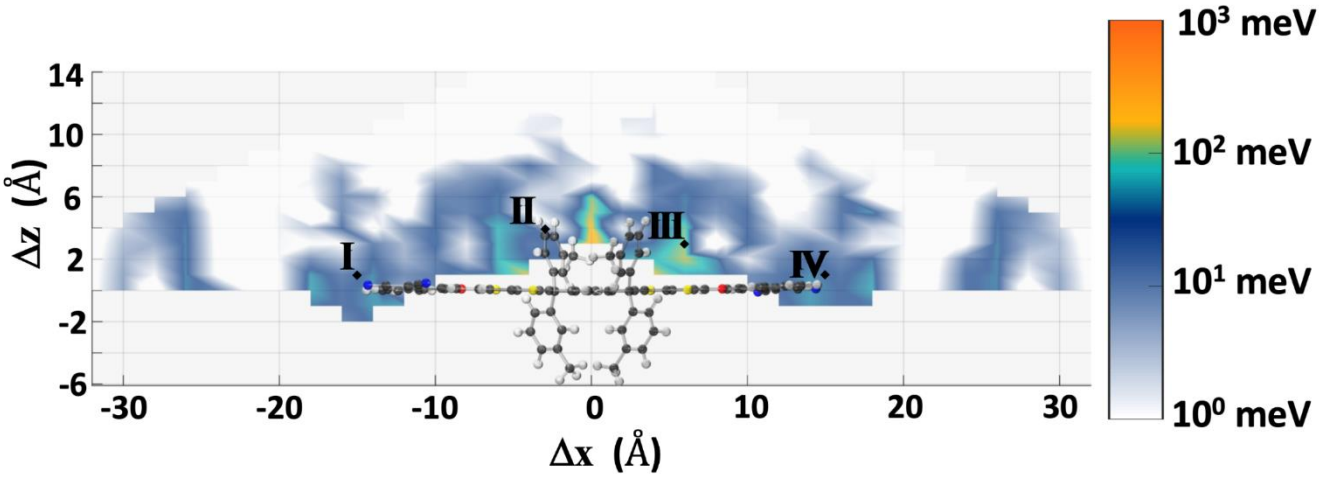

Figure 10. Electronic coupling |*J*| in an ***m*-ITIC-C1** dimer. Each colored pixel represents a coupling at a given π-stacking distance (Δz) and slip distance (Δx). The four minimum energy geometries (labeled I, II, III, IV) on top of the coupling values correspond to the geometries in the xz-plane (see **Figure 8** for dimer geometries). Smaller degrees of slip can produce stacked geometries (III) that have electronic couplings near 100 meV. Thermal disorder would afford much smaller average crystalline couplings, nearer to those in **Table 1**.

Naphthyl End Groups

ITN-C9 Crystal Structure[8b] **(Figure 11A)**

Single Molecule Conformation and Crystal Packing. Crystals of **ITN-C9** suitable for diffraction studies were grown by vapor phase diffusion of acetone into a CH_2Br_2 solution. **ITN-C9** packs in a triclinic lattice and exhibits a planar conformation with D_{SO} = 2.79 Å and a small end group-IDTT core torsion (φ = 3.7°). Similar to most other IDTT type acceptors, **ITN-C9** packs in a face-to-face, slip-stacked fashion with π-π stacking along the *a* crystallographic axis, with stacks of molecules insulated from each other by their alkyl chains. The end groups exhibit π-π distances of 3.39 Å and 3.50 Å, corresponding to D_{cent} = 21.68 Å and 26.32 Å. These large centroid-centroid distances reflect the increased size of the end groups. **ITN-C9** also exhibits a large D_{core} (> 7 Å).

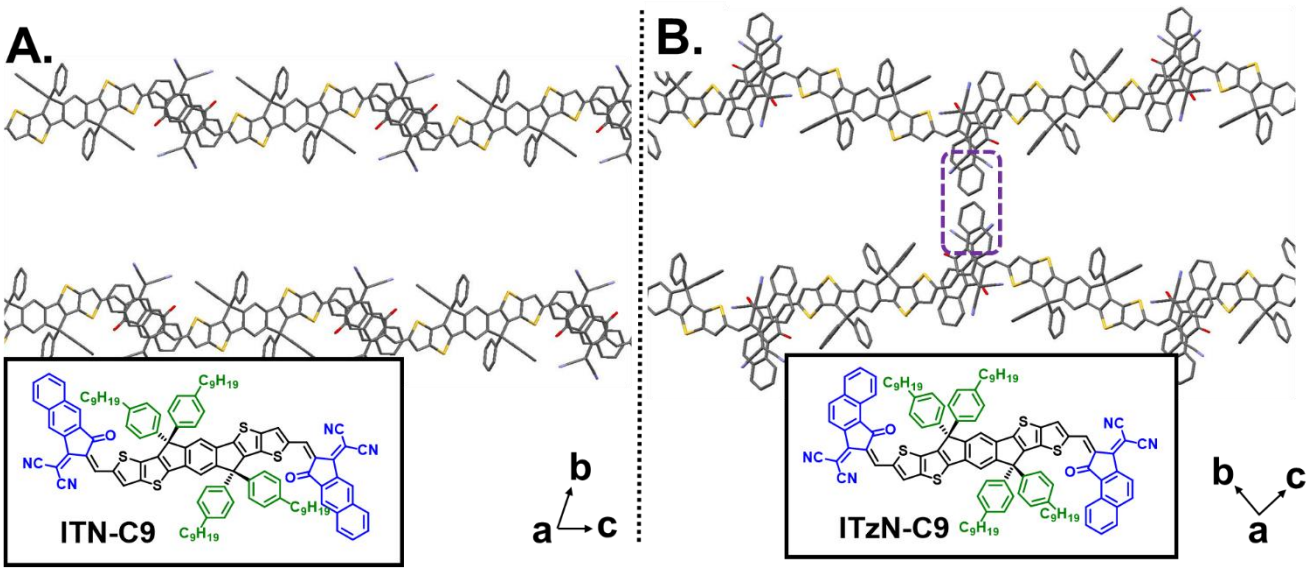

Figure 11. Crystal structure packing diagram of **A. ITN-C9** viewed along the *a* crystallographic axis and **B. ITzN-C9** viewed along the *a* crystallographic axis with the location of H-bonding and interstack π-π interactions boxed in purple. Alkyl chains have been omitted for clarity, sulfur is yellow, oxygen is red, and nitrogen is blue.

Computational Analysis of Single Molecules and Crystal Packing. Computation of the MOs of the ITN molecule at the B3LYP/DZP level (see SI computational methods) indicates that the end groups contribute substantially to the LUMO, whereas the HOMO is primarily localized on the IDTT core.[8b] This localization of the LUMO on the end groups is vital to charge transporting properties because **ITN-C9** assembles such that the end groups stack with short π-π distances (3.4-3.5 Å) while the IDTT cores are considerably further apart (D_{core} > 7 Å). The DOS of the **ITN-C9** single crystal structure was calculated,[32b] revealing a significant contribution of the naphthyl end group to the conduction band (52%), further highlighting the importance of the end group π-π stacking. Electronic coupling computations (ZINDO/S; see SI computational methods) of a nearest neighbor

minimal cell revealed |*J*| values of 5.85 meV and 1.49 meV. Charge transport in crystalline domains of **ITN-C9** is limited by the absence of |*J*| couplings along the *b* crystallographic axis.

ITzN-C9 Crystal Structure[8b] **(Figure 11B)**

Single Molecule Conformation and Crystal Packing. Crystals of **ITzN-C9** suitable for diffraction studies were grown by vapor phase diffusion of acetone into a CH_2Br_2 solution. **ITzN-C9** packs in a triclinic lattice with D_{SO} = 2.62 Å and 2.75 Å and corresponding φ = 7.4° and 1.9°. **ITzN-C9** packs in a face-to-face, slip-stacked fashion with π-π stacking along the *a* crystallographic axis. Interestingly however, the angled naphthyl end groups of **ITzN-C9** allow for additional π−π interactions (3.55 Å, 3.93 Å) and hydrogen bonding interactions (Ar-H···NΞC, 2.63 Å, 3.18 Å) between stacks of acceptor (see reference 25 additional packing diagrams). Within stacks of the molecules, the end groups exhibited π-π distances of 3.31 Å and 3.39 Å and corresponding D_{cent} = 19.81 Å and 23.94 Å. **ITzN-C9** also exhibits a large D_{core} (7 Å).

Computational Analysis of Single Molecules and Crystal Packing. As with **ITN-C9**, MO computations at the single molecule level (B3LYP/DZP; see SI computational methods) indicate that the end groups contribute substantially to the LUMO, whereas the HOMO is primarily localized on the IDTT core.[8b] DOS calculations[32b] reveals an even greater contribution of the naphthyl end group to the conduction band (69%) than in I**TN-C9** (52%). **ITzN-C9** exhibited both large |*J*| values (end group π-π interacting neighbors: 38.17 meV and 5.32 meV) and the possibility of greater charge transport dimensionality than **ITN-C9** due to the presence of additional coupling neighbors along the *b* crystallographic axis. As with **ITN-C9** |*J*| value calculations were carried out at the ZINDO/S (described in SI computational methods) level over a minimal cell of all nearest neighbors.

Fluorinated End Groups

ITIC-C6-4F Crystal Structure[8a] **(Figure 12)**

Single Molecule Conformation and Crystal Packing. Crystals of **ITIC-C6-4F** suitable for diffraction studies were grown by vapor phase diffusion of *n*-heptane into a CH_2Br_2 solution. **ITIC-C6-4F** packs in a triclinic lattice with D_{SO} = 2.71 Å and 2.82 Å and corresponding large end group to IDTT core torsions (φ = 10.1° and 7.9°). Interestingly, **ITIC-C6-4F** exhibits a hybrid packing motif in which a face-to-face packing coexists with the edge-to-face packing motif observed in **ITIC** polymorph 2. The face-to-face pairs of molecules exhibit short π-π distances of 3.35 Å (D_{cent} = 21.56 Å), while the edge-to-face pairs exhibit a $D_{S\pi}$ = 3.21 Å (D_{cent} = 7.71 Å). As seen in **ITIC** polymorph 2, the edge-to-face packing is also driven by H-bonding interactions between end group aryl protons and end group nitrile and carbonyl lone pairs (Ar-H···NΞC and Ar-H···O=C), with interaction distances of 2.58 Å and 2.39 Å, respectively. These shorter interaction distances relative to **ITIC** polymorph 2 reflect the inductive, electron withdrawing nature of the fluorine atoms adjacent to the H-bonding hydrogens.

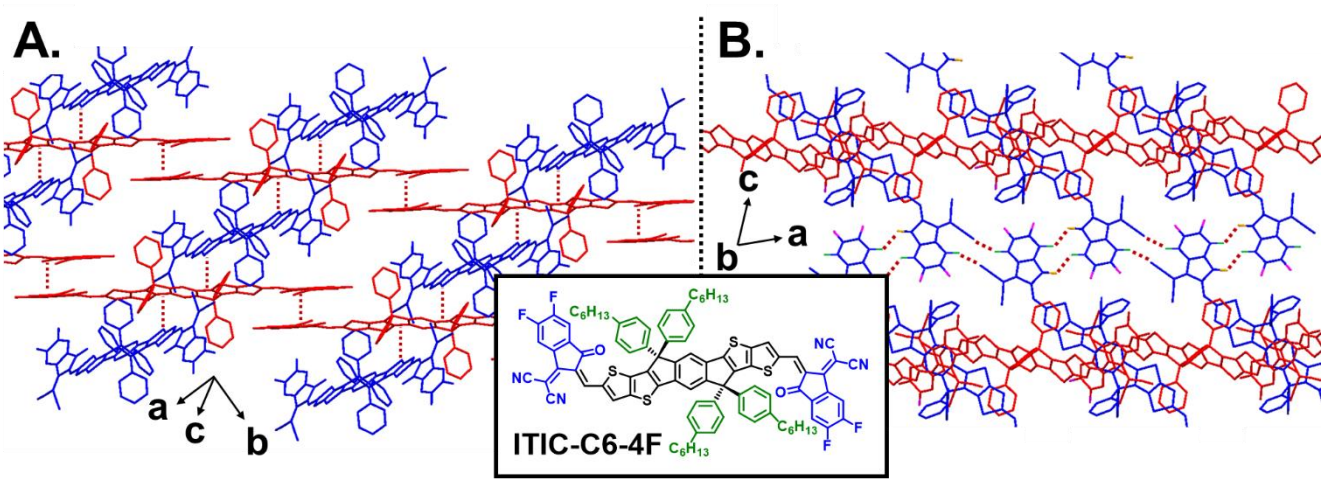

Figure 12. Crystal structure packing of **ITIC-C6-4F** viewed along **A.** the *c* crystallographic axis, and **B.** the *b* crystallographic axis. Molecules packing along the *a*/*b* crystallographic axis are shown in red, and molecules packing along the *c* axis are shown in blue. Alkyl chains are omitted for clarity. S···π, π-π, and H-bonding interactions are shown with red dashed lines. In panel B, fluorine atoms are shown in magenta and H-bonding hydrogens and oxygens are shown in green and orange, respectively. The structure of **ITIC-C6-4F** is shown for convenience.

Computational Analysis of Crystal Packing. The greatest |*J*| was observed between the reference and its edge-to-face neighbor (|*J*|=17.1 meV), whereas the π-π interaction between the reference and its face-to-face neighbor yield a |*J*| value of 2.8 meV. Note that the edge-to-face interaction is similar in magnitude to the edge-to-face polymorph of **ITIC** (16 meV). From a qualitative viewpoint, the seemingly highly interconnected crystal structure packing of **ITIC-C6-4F** may be expected to favor isotropic charge transport. However, upon summing all |*J*| contributions along each crystallographic axis it is revealed that **ITIC-C6-4F** exhibits a high degree electronic coupling anisotropy, with ~90% of its electronic coupling along the *a* crystallographic axis and the remaining 10% along the *b* crystallographic axis.

The band structure of **ITIC-C6-4F** (**Figure 13**) shows more anisotropy than **ITIC** polymorph 1. The anisotropy is greatest from the Γ-point (origin) to the X (1/2,0,0), which corresponds well to the high-degree of coupling along *a*. The DOS for **ITIC-C6-4F** shows the expected shift in the valence band energy as well as the broadening of the conduction band energies. The broadening speaks to the increased end group coupling between the π-stacked units in the crystal structure.

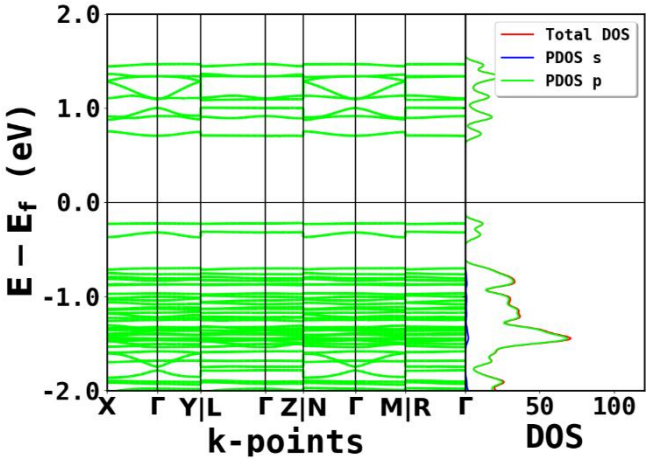

Figure 13. The band structure and DOS of **ITIC-C6-4F**. The Fermi energy (E_f) is defined from the middle of the "HOMO-LUMO" band gap. The high-symmetry k-points of the triclinic lattice are plotted from the Γ-point (origin) towards the listed lattice directions. The DOS is projected onto s and the three p orbitals with the total DOS being the sum of the four orbitals.

ITIC-C4-4F Crystal Structure (Figure 14A)

Single Molecule Conformation and Crystal Packing. Crystals of **ITIC-C4-4F** suitable for diffraction studies were grown by vapor phase diffusion of *n*-heptane into a CH_2Br_2 solution. **ITIC-C4-4F** packs in a triclinic lattice and exhibits a planar conformation with D_{SO} = 2.70 Å and φ = 0.6°. Interestingly, the shorter alkyl chains in **ITIC-C4-4F** relative to **ITIC-C6-4F** results in face-to-face, slip-stacked packing motif with π-π distances as short as 3.28 Å and a short corresponding D_{cent} = 15.92 Å. π-π interactions along the *a* axis that are present within columns of molecules, as well as H···F interactions[35] (2.52 Å) between their end groups that are less than the sum of their Van der Waals radii, connect the stacks of molecules. This interaction is expected to stabilize the face-to-face packing observed. **ITIC-C4-4F** also exhibits a D_{core} >7 Å.

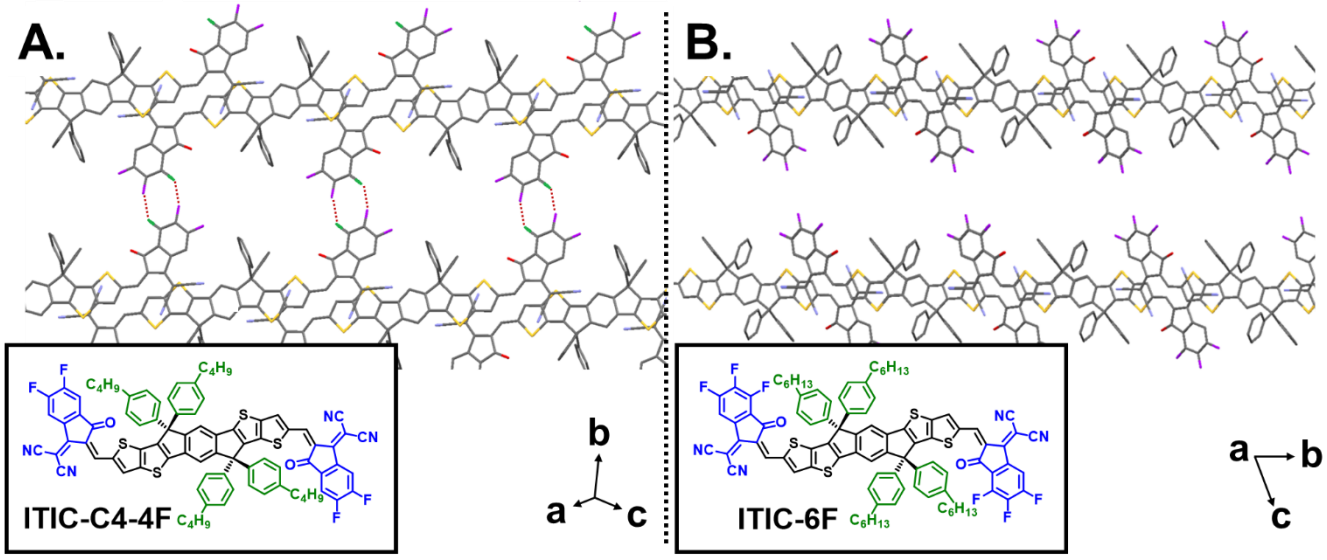

Figure 14. Crystal structure packing of **A. ITIC-C4-4F** viewed along the *a* crystallographic axis with H···F interactions shown in red and H···F interacting hydrogens shown in green and **B. ITIC-6F** viewed along the *a* crystallographic axis. In both panels sulfur is yellow, oxygen is red, nitrogen is blue, fluorine is magenta, and alkyl chains have been omitted for clarity.

Computational Analysis of Crystal Packing. The computational analysis of **ITIC-C4-4F** shows that dispersion energy density of the unit cell is E_{disp}= -197 kcal/cm^3, which is the strongest dispersion energy of the fluorinated **ITIC** derivatives. Only the shorter side chain **ITIC-C3** and the structural isomer ***m*-ITIC-C6** have a stronger E_{disp}. From **Table 1**, there is a clear trend of larger dispersion interactions with shorter side chains due to the greater through-space interactions of both Van der Waals and H-bond interactions, due to the tighter packing and greater number of interactions. The DOS and band structure (**Figures S13-S14**) confirms the stronger interactions with the band broadening due to the dispersion interactions along the *b* axis.

ITIC-6F Crystal Structure[8a] **(Figure 14B)**

Single Molecule Conformation and Crystal Packing. Crystals of **ITIC-6F** suitable for diffraction studies were grown by vapor phase diffusion of *n*-heptane into a CH_2Br_2 solution. **ITIC-6F** packs in a triclinic lattice and exhibits a planar conformation with D_{SO} = 2.70 Å and φ = 0.8°. **ITIC-6F** packs in a face-to-face, slip-stacked fashion with π-π distances of 3.95 Å and 3.28 Å and corresponding D_{cent} = 15.83 Å and 19.94 Å. In addition, a very short C≡N···π (end group) interaction is present (3.16 Å), which appear to reflect the favorable electrostatic interactions between the CN lone pair and the highly fluorinated electron deficient end group. **ITIC-6F** also exhibits a D_{core} >7 Å.

Computational Analysis of Crystal Packing. **ITIC-6F** exhibits a remarkably large electronic coupling (|*J*|=56.8 meV) between the reference molecule and its CN···π interacting neighbor, highlighting the importance of the nitrile groups in directing packing and intermolecular forces. The |J| between the reference and its close π-π neighbor (3.28 Å) also resulted in a large electronic coupling (|*J*|=45.2 meV). Summing these contributions along the different crystallographic axes, it is observed that **ITIC-6F** exhibits a greater degree of |*J*| isotropy than **ITIC-C6-4F**, with 70% of its electronic coupling along the *b* axis and 30% along the *a* axis.

The DOS of **ITIC-6F** (**Figure 15**) shows similar conduction band broadening as **ITIC-C6-4F** due to the end group coupling. The valence band does show a high-degree of broadening, especially near the band edges of the HOMO and LUMO, likely due to the tighter intermolecular coupling of the π and π* orbitals created by the high intramolecular polarization of the IDTT core due to the fluorination of the end groups.

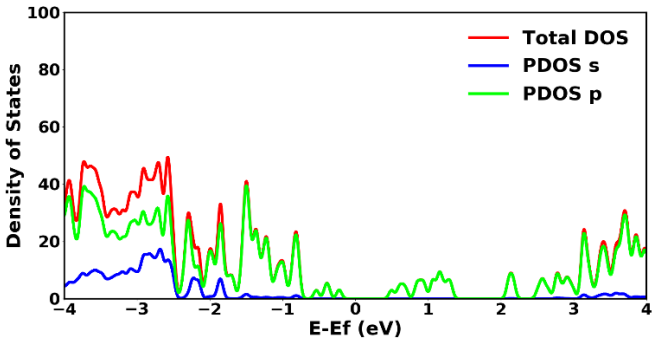

Figure 15. DOS of the **ITIC-C6-6F** crystal structure. The fluorination of the end groups shows the valence and conduction bands hybridize due to intermolecular coupling interactions along the *b* crystallographic axis.

Discussion and Conclusions

Although correlating acceptor single crystal structure features with performance trends in BHJ solar cells can be challenging due to the many factors influencing film morphology (solvent, processing methodology, donor choice), systematic analysis of IDTT crystal structures provides a detailed picture of the low energy configurations available to these molecules as electron conducting pathways. In addition, those factors that influence the packing motif and the strength of the local interactions of these small molecule acceptors have now been documented and coarse rational design trends can be extrapolated from the crystallographic structural and electronic structural data.

It is found that IDTT acceptors can organize in two basic crystallization motifs: edge-to-face or face-to-face. Edge-to-face packing is driven by S···π interactions between the cores of two acceptor molecules and H-bonding interactions (Ar-H···NΞC and Ar-H···O=C) between the end groups, whereas as face-to-face packing is driven primarily by π-π interactions between end groups or between an end group and an IDTT core, although H-bonding interactions (Ar-H···NΞC) were also observed in some face-to-face structures. Of the molecules that exhibit edge-to-face packing, specifically **ITIC** polymorph 2 and **ITIC-C6-4F** (**Figures 5B** and **12**, respectively), relatively large J values, 16 – 17 meV, are computed from the S···π interactions. However, in edge-to-face packing the acceptor can only transport charge along a 1D path, limiting charge transport dimensionality and overall charge mobility.[7b, 8a] In face-to-face packing, stacked columns or interleaved bricks of π-stacked molecules form, which lends them to greater charge transport directionality,[8a] and as a result, greater overall carrier mobility.[7b] Note, that a greater dispersity in *J* values is found in π-π interactions, 1.49 – 56.8 meV, indicating that the capacity of π-π interactions to support charge transport depends strongly on the distance and orientation of the π planes involved. In addition, thermally activated acoustic modes within the crystal as well as thermal defects may lead to dynamic changes in J, while some larger values can be activated, the thermal average is likely to lower the overall value from the maximum J.

In thin films and in BHJ active layers, where film formation is rapid (disordered and metastable molecular arrangements exist),[36] both edge-to-face and face-to-face packing motifs can potentially co-exist, since they are minimum energy modes of interaction. Although edge-to-face packing has only been directly observed in **ITIC** and **ITIC-C6-4F**, it is reasonable to posit that edge-to-face packing can exist in other IDTT acceptors because of their shared core structure. The proportion of these two packing motifs in thin films is related to the thermodynamics and kinetics of film formation. Qualitatively, face-to-face packing seems to be more favorable thermodynamically as it is stabilized by strong intermolecular interactions (H-bonding, π-π interactions), as well as kinetically, as edge-to-face packing requires a more specific geometric arrangement of the molecules. Experimental results indicate that face-to-face packing is the dominant form of packing in IDTT acceptors, as it has been observed directly in thin films through GIWAXS[8b, 10] and is present in all but one of the nine crystal structures of IDTT acceptors analyzed here. Other factors inherent to the devices can almost certainly play a role as well. When energetic differences between packing motifs is small, surfaces can break the symmetry within the crystals leading to the abundance of face-on orientations in thin films. In addition, molecular dynamics simulations modeling **ITIC** thin films have indicated that face-to-face packing is the dominant form of packing in thin films, with 70% of the molecules in the simulation containing end group π-π interactions.[7b]

In addition to understanding the different modes of packing available to IDTT acceptors, and how these packing motifs differ in terms of charge transporting properties, analysis of the IDTT crystal structures presented here provides additional information for correlating side chain and end group properties with the various intra/inter-molecular interactions observed in the crystal structures. Planarity promoting[28] S···O interaction distances remained relatively consistent (2.66 – 2.82 Å) across the series, although **ITIC** polymorph 1 exhibits both the shortest (2.66 Å) and second longest (2.80 Å) D_{SO}, suggesting that D_{SO} is not readily relatable to the molecular structure. φ was also not found to depend strongly on end group or alkyl chain the identity, although the magnitude of φ correlates strongly with the observed packing motif. Both **ITIC-C6-4F** and **ITIC** polymorph 2, which pack at least in part in an edge-to-face fashion (**Figures 12** and **5B**, respectively), exhibit large core-end group torsions (φ = 10.1° and 13.4°, respectively). This result indicates that in a less conjugated conformation π-π stacking between end groups is less favorable. D_{cent} correlates well with the polarity of the end group, with higher levels of fluorination resulting in smaller D_{cent}. This is likely due to increasing dispersion interactions due to the higher electron densities of the halogen groups as well as increasing polarization between the electron deficient end groups and the electron rich IDTT cores, coaxing the molecules to pack more tightly and with greater overlap through electrostatic interactions (*e.g.*, see **ITIC-6F** *vs.* **ITIC-C6-4F** *vs.* **ITIC-C4-4F** *vs.* **ITIC** in **Table 1**). Although it may be tempting to attribute the decreased D_{cent} of **ITIC-C4-4F** relative to **ITIC-C6-4F** to alkyl chain truncation, alkyl chain shortening does not affect the D_{cent} of **ITIC-C3** *vs.* **ITIC**. However, alkyl chain length can influence the packing motif adopted, as **ITIC-C4-4F** packs in the more common face-to-face packing motif, whereas **ITIC-C6-4F** packs in a hybrid edge-to-face/face-to-face packing motif. This is likely the result of decreased alkyl chain volume, allowing for tighter π-π interactions (which is reflected in the greater E_{disp}, **Table 1**) and also permitting decreased distance between

columns of molecules, allowing H···F interactions without losing π-π interactions within columns of molecules (**Figure 12**). This is also in line with the PES calculations performed for ***m*-ITIC-CX** (*vide supra*, **Figure 9**) which shows that alkyl chain lengthening both disrupts the π-π stacking distance and disrupts planarity between the end groups and IDTT core, thus promoting edge-to-face packing. This dramatic change in crystal structure packing highlights the delicate balance of intermolecular forces that govern the packing motif adopted. Alkyl chain repositioning from the *para* to the *meta* position leads to a shorter D_{cent} (see **ITIC** polymorph 1 *vs.* ***m*-ITIC-C6** in **Table 1**). This contraction is counterintuitive and the origin is unclear presently. The interplay between the alkyl chain length and alkyl chain position can be subtle with respect to packing distances. Increasing the size of the end group in a linear fashion results in longer D_{cent} in **ITN-C9**, whereas the kinked π-extended **ITzN-C9** has a similar D_{cent} as **ITIC**, indicating the geometry of the end group as well as the size is important in determining D_{cent}.

Overall, a careful joint theory-experimental analysis of IDTT crystal structures yields three principle design insights. First, increasing the polarization between the end group and IDTT core through end group fluorination leads to tighter face-to-face π-π interactions. We find an increased E_{disp} (**Table 1**) as the density of fluorination increases that is attributed to increased Van der Waals interactions. Second, because edge-to-face packing in IDTT acceptors is stabilized by H-bonding interactions between the end groups (*vide supra*), controlling the strength and number of H-bonding interactions between end groups may serve as a handle to control the propensity of a molecule to pack in an edge-to-face fashion. Third, face-to-face π-π interactions are also stabilized by additional H-bonding/H···F interactions enabled by end groups with the appropriate geometry (**ITzN-C9**), sufficiently short alkyl chains (**ITIC-C4-4F**), or alkyl chains in the correct position (***m*-ITIC-C6**). Although H-bonding/H···F interactions in face-to-face packing is not a general phenomenon, their presence in the crystal structures of **ITzN-C9**, **ITIC-C4-4F**, and ***m*-ITIC-C6** suggests that by tuning the shape of the end group or the length/position of the alkyl chain (as opposed to changing the DOS of the end group), H-bonding/H···F interactions can promote co-planar, face-to-face packing.

Analyzing the results presented here in the context of fullerene acceptors and PDI acceptors (two of the most widely used electron acceptors for OSCs) elucidates many of the morphological reasons underlying the success of IDTT acceptors in replacing fullerenes, as well as the reasons underlying the inability of PDI acceptors to match the performance of IDTT acceptors (**Figure 16**). Taken together, these results also lead to general design rules for OSC electron acceptors (*vide infra*). Fullerene acceptors have enjoyed great success due to their ability to form well connected and strongly coupled domains [**$PC_{61}BM$**: 12 meV[37] (amorphous), 50 meV[38] (crystalline)] during the rapid and uncontrolled BHJ film formation process. This is made possible by their spherical shape, which allows for them to pack such that each molecule is electronically coupled to ~6 neighbors, resulting in highly redundant molecular networks and isotropic charge transport.[39] The high redundancy is particularly important as it makes fullerene acceptor networks resilient to defects, as no single charge transport pathway is critical to charge extraction.

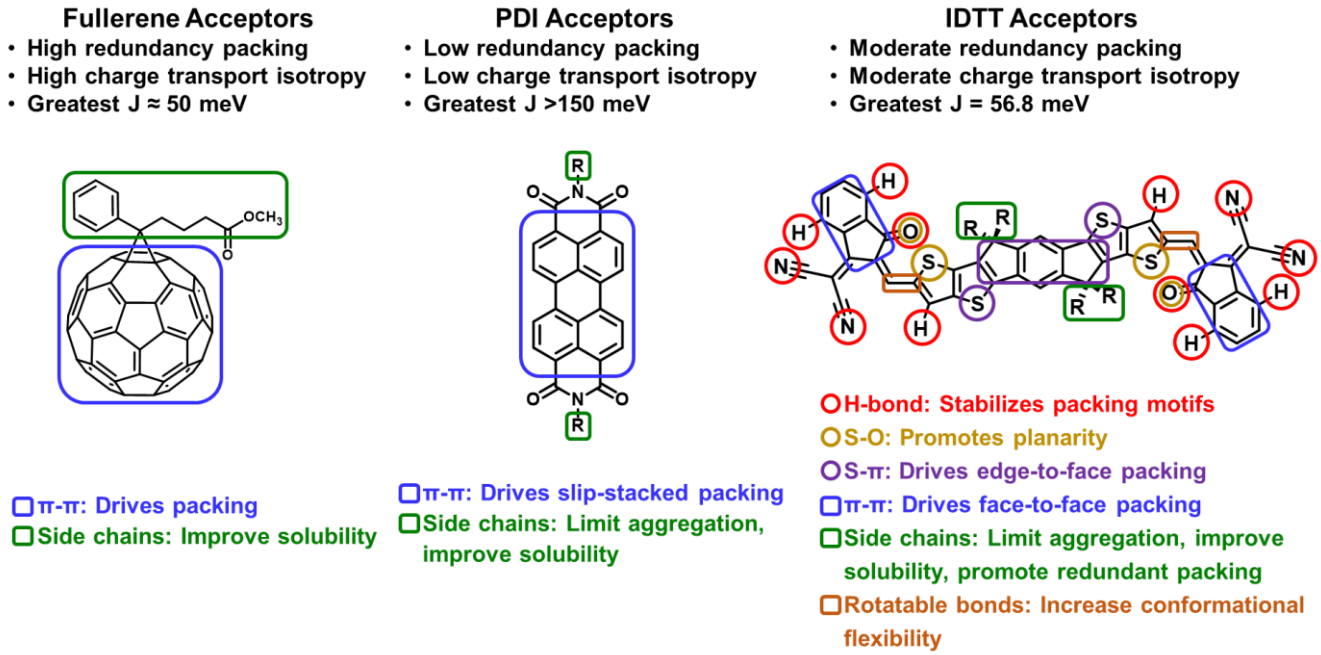

Figure 16. Relationships between structure, intra/inter-molecular forces, and packing of fullerene acceptors, PDI acceptors, and IDTT acceptors.

Crystal structures of monomeric PDI type acceptors[7d, 7e, 40] reveal that monomeric PDIs pack almost exclusively in a slip-stacked fashion, with substantial overlap between the molecular cores. Although this high degree of overlap can afford very large electronic coupling values (|*J*|>150 meV),[40a, 41] the slip-stacked packing motif only allows each PDI molecule to couple appreciably with two other molecules. This lack of coupling redundancy makes for a very fragile charge transporting network,[39] where a single defect in molecular packing can result in segregated domains that trap charges and induce

recombination. This highlights an inherent limitation of PDI type acceptors. The tremendous driving force to maximize π-π interactions leads to approximately eclipsed packing and because of the lack of functionalities in place to inhibit this packing or promote other modes of packing, monomeric PDIs will always predominately adopt this non-redundant form of packing. This is problematic not only in terms of forming redundant electronic networks, but also gives rise to the well documented morphological issue of over-aggregation/crystallization[42] associated with monomeric PDI acceptors. As a solution, researchers have developed many multimeric PDI acceptors[42] which have been successful in controlling PDI domain size. Although exceptions may exist,[43] this strategy is not generally expected to greatly improve redundancy or charge transport dimensionality, as multimeric PDIs are typically electronically similar to a cluster of monomeric PDIs (due to their highly twisted structures), with each PDI unit only able to form π-π interactions with two other PDI units. This is born out in the crystal structure of a dimeric PDI acceptor[44] in which each PDI unit is found to only interact with two other PDI units. Because of the large torsion (66°) between PDI units within the dimer, this results in non-redundant, 1D charge transporting networks similar to monomeric PDI acceptors. Unfortunately however, single crystal XRD structures for multimeric PDI acceptors are rare,[43d, 44] so a detailed understanding of the packing and interactions present in organized domains, as well as their implications on charge transport and OSC acceptor design, is not possible.

When packing in the more common face-to-face fashion, IDTT acceptors can couple electronically with >4 neighbor molecules through end group overlap (J values from crystal structures range from 1.49 – 56.8 meV). This creates redundancies in charge transport pathways, making face-to-face packed IDTT acceptor networks likely to be resilient to defects, similar to what is seen in fullerene acceptors. Note that this redundant form of packing is made possible by the sp^3 centers on the IDTT core where the alkyl phenyl substituents are appended. By preventing molecules from packing in an eclipsed/cofacial configuration (as seen with PDI acceptors), this allows each molecule to interact with more neighbors through π-π interactions of the LUMO-rich end groups (*vide supra*), while also preventing over-aggregation/crystallization. Although the magnitude of the electronic couplings calculated for IDTT acceptors (up to ~56 meV) is generally less than PDI acceptors (>150 meV), the ability to form well-connected, redundant networks is likely more important. In addition, the computed PES of ***m*-ITIC-C6** (*vide supra*, **Figure 9**) indicates that many orientations/geometries of the end groups can be accommodated in face-to-face packing while still maintaining strong electronic coupling, which is beneficial for forming electronically connected domains in disordered BHJs. Furthermore, IDTT acceptors possess the ability to pack in an alternative, well-defined and fairly strong coupling (~15 meV) motif: edge-to-face packing. While edge-to-face packing does not provide as great charge transport dimensionality or redundancy as face-to-face packing, it may help reduce the formation non-conducting defects between microcrystalline domains e.g. grain boundary healing. The ability of IDTT acceptors to pack in both motifs (**ITIC** poly 1 and **ITIC** poly 2), and for both motifs to coexist in a single crystal structure (**ITIC-C6-4F**) indicates that they are likely close in energy, which is enabled by the diverse functionalities contained within IDTT acceptors and the wide array of intra/inter-molecular interactions present (**Figure 16**). In addition, the flexibility of IDTT acceptors to accommodate torsions between the core and the end groups, and the presence of the sp^3 centers (as noted above) are also important. Together, the lenient geometric requirements, strongly electronically coupling, and redundant networks afforded by face-to-face packing, as well as the flexibility of IDTT acceptors to pack in the strongly coupling edge-to-face packing motifs allows IDTT acceptors to compensate for their less favorable topology relative to fullerene acceptors.

Generalizing the above observations, design rules for producing small molecule electron acceptors that self-assemble into electronically robust and well-connected networks can be derived and are as follows:

1) Acceptors should present multiple sites for π-interaction that are separated spatially and/or sterically but are in conjugation with each other.

Segregating π-surfaces promotes the formation of redundant networks that are resistant to defects and improves the possibility for high isotropy charge transport. In fullerene based acceptors, this is accomplished by the unique, spherical molecular topology, and in IDTT acceptors the alkyl phenyl containing sp^3 centers segregate the π-surfaces sterically. The presence of only a single site for π-interactions limits the ability of PDI acceptors to produce redundant networks.

2) Large, planar, and exposed π-surfaces should be avoided.

The large, exposed π-surface inherent to PDI acceptors has plagued them with issues of over-aggregation, which limit solar cell short circuit currents and fill factors. Furthermore, the tremendously large J values afforded by interaction of these large π-surfaces has shown to be unnecessary for high performance solar cells. Both fullerene acceptors and IDTT acceptors exhibit more moderate J values in comparison to PDI acceptors, but typically exhibit similar or greater short circuit currents and fill factors. This suggests that high redundancy packing with moderate J values is more favorable than low redundancy packing with large J values.

3) A variety of functional groups and some conformational flexibility may help accommodate disorder in BHJ films.

IDTT acceptors are unique among the three classes of acceptors analyzed here in that they are densely functionalized with a variety of groups. As observed in the crystal structures and depicted in **Figure 16**, this leads to variety of possible stabilizing interactions, such as H-bonding, S···π, π-π, and electrostatic interactions. It is likely that in rapid and uncontrolled BHJ film formation processes these interactions help facilitate organization of the IDTT acceptor molecules into one of the energetic minima available to them. The most striking example of this is the presence of an edge-to-face packing motif. Although it is unlikely that edge-to-face packing is dominant in the BHJ (*vide supra*), edge-to-face packing provides a pathway for acceptor molecules to organize with strong electronic coupling with each other when face-to-face packing is not possible due to the kinetics of film formation. Similarly, the flexibility of IDTT acceptors to accommodate torsions between the end groups and the core (up to ~8° in face-to-face packing and ~10-13° in edge-to-face packing) is expected to be aid in the formation of well-connected domains when planarity cannot be accommodated. This flexibility is balanced by S···O interactions that promote molecular planarity and conjugation between the end groups and the core.

In conclusion, this study sheds light on the widespread success of IDTT acceptors in forming favorable BHJ morphologies by elucidating the role of each functionality in molecular packing at a greater level of precision and detail than previously reported. IDTT acceptor crystal structures exhibit a delicate balance of intra/inter-molecular forces, which in the BHJ allows them to self-assemble in pure, mesoscale, well-connected networks that are resilient to defects. In addition, IDTT acceptors are able to

accommodate disorder inherent in BHJs due to their conformational flexibility and their flexibility to pack in different motifs. Single crystal XRD structures capture these many, and at times unexpected, forces that drive the exquisite and robust packing of IDTT type acceptors. Further analysis of these crystal structures through computation provides quantitative metrics to understand how variations in chemical structure and crystal packing affect the electronic structure of organized domains of IDTT acceptors. These findings were used to construct design rules for IDTT acceptors, as well as general design rules for small molecule acceptors of OSCs.

Experimental

Additional details regarding computation, synthesis, and x-ray crystallography can be found in the supporting information.

X-Ray Crystallography:

ITIC-C3: Crystal Growth: ITIC-C3 (5 mg) was dissolved CBr_2H_2 (1 mL) in a 2 mL vial that was then placed in a 40 mL vial containing *n*-heptane (~5 mL). The larger vial was then tightly capped and left undisturbed for several weeks, at which point diffraction quality crystals were collected.

Crystal Data for $C_{84}H_{62}Br_4N_4O_2S_4$ (*M* =1607.25): monoclinic, space group C2/c (no. 15), a = 72.948(4) Å, b = 8.3087(5) Å, c = 29.0233(18) Å, β = 108.868(4)°, V = 16645.9(18) Å^3, Z = 8, T = 100.0 K, μ(MoKα) = 2.080 mm^{-1}, *Dcalc* = 1.283 g/mm^3, 82543 reflections measured (2.966 ≤ 2Θ ≤ 53.164), 17154 unique (R_{int} = 0.2354, R_{sigma} = 0.2364) which were used in all calculations. The final R_1 was 0.1447 (I > 2σ(I)) and wR_2 was 0.4017 (all data). Cambridge Crystallographic Database Deposition Number: 1946199

***m*-ITIC-C6: Crystal Growth**: ***m*-ITIC-C6** (5 mg) was dissolved CBr_2H_2 (1 mL) in a 2 mL vial that was then placed in a 40 mL vial containing *n*-heptane (~5 mL). The larger vial was then tightly capped and left undisturbed for several weeks, at which point diffraction quality crystals were collected.
Crystal Data for $C_{96}H_{86}Br_4N_4O_2S_4$ (*M* =1775.56): triclinic, space group P-1 (no. 2), a = 8.7888(3) Å, b = 18.7534(6) Å, c = 25.5301(8) Å, α = 88.9873(19)°, β = 88.2993(19)°, γ = 81.2251(17)°, V = 4156.4(2) Å^3, Z = 2, T = 100.0 K, μ(MoKα) = 2.090 mm^{-1}, *Dcalc* = 1.419 g/mm^3, 53996 reflections measured (1.596 ≤ 2Θ ≤ 56.69), 20506 unique (R_{int} = 0.0451, R_{sigma} = 0.0650) which were used in all calculations. The final R_1 was 0.1246 (I > 2σ(I)) and wR_2 was 0.4018 (all data).
Cambridge Crystallographic Database Deposition Number: 1946200

ITIC-C4-4FCrystal Growth: **ITIC-C4-4F** (5 mg) was dissolved CBr_2H_2 (1 mL) in a 2 mL vial that was then placed in a 40 mL vial containing *n*-heptane (~5 mL). The larger vial was then tightly capped and left undisturbed for several weeks, at which point diffraction quality crystals were collected.

Crystal Data for $C_{86}H_{62}F_4N_4O_2S_4$ (*M* =1387.63): triclinic, space group P-1 (no. 2), a = 8.3753(3) Å, b = 15.1244(6) Å, c = 15.4292(6) Å, α = 81.129(2)°, β = 77.787(2)°, γ = 87.875(2)°, V = 1887.34(13) Å^3, Z = 1, T = 99.87 K, μ(CuKα) = 1.640 mm^{-1}, *Dcalc* = 1.221 g/mm^3, 19822 reflections measured (7.722 ≤ 2Θ ≤ 127.362), 6110 unique (R_{int} = 0.0305, R_{sigma} = 0.0309) which were used in all calculations. The final R_1 was 0.0753 (I > 2σ(I)) and wR_2 was 0.2057 (all data). Cambridge Crystallographic Database Deposition Number: 1946198

Computational Analysis:

Single Crystal Periodic Computational Details: All single crystal calculations were performed in the Vienna ab-initio simulation package (VASP), version 5.4.1) with DFT using the Perdew-Burke-Ernzerhof (PBE) functional; Grimme's dispersion (PBE-D2) was applied to determine the van der Waals interactions in the single crystals. Solvent and ions were removed prior to calculation and the crystals were not optimized. No smearing was included. The planewave cutoff energy was 400 eV. A calculation typically used a Gamma-centered mesh of k-points of 5×3×3 for the static calculations. Electron coupling calculations (*J*) between a reference molecule and its nearest neighbors in the single crystals, transfer integrals, selected optimized geometries and PES calculations of dimers were computed at the DFT/ZINDO/S levels. See supporting information Section 5 for further details.

Acknowledgements

This work was supported as part of the Center for Light Energy Activated Redox Processes (LEAP), an Energy Frontier Research Center funded by the U.S. Department of Energy, Office of Science, Basic Energy Sciences under Award # DE-SC0001059. S.M.S and T.J.A thank the NSF for Predoctoral Research Fellowships.

Keywords: Solar Cells • Non-Fullerene • Crystal Structure • Molecular Modelling

References

[1] a) S. B. Darling, F. You, *RSC Advances* **2013**, *3*, 17633-17648; b) K. A. Mazzio, C. K. Luscombe, *Chemical Society Reviews* **2015**, *44*, 78-90; c) L. Lu, T. Zheng, Q. Wu, A. M. Schneider, D. Zhao, L. Yu, *Chem. Rev.* **2015**, *115*, 12666-12731.

[2] a) J. Yuan, Y. Zhang, L. Zhou, G. Zhang, H.-L. Yip, T.-K. Lau, X. Lu, C. Zhu, H. Peng, P. A. Johnson, M. Leclerc, Y. Cao, J. Ulanski, Y. Li, Y. Zou, *Joule* **2019**, *3*, 1140-1151; b) Q. An, X. Ma, J. Gao, F. Zhang, *Science Bulletin* **2019**, *64*, 504-506.

[3] a) J. Hou, O. Inganäs, R. H. Friend, F. Gao, *Nat. Mater.* **2018**, *17*, 119; b) S. M. McAfee, J. M. Topple, I. G. Hill, G. C. Welch, *J. Mater. Chem. A* **2015**, *3*, 16393-16408; c) A. Wadsworth, M. Moser, A. Marks, M. S. Little, N. Gasparini, C. J. Brabec, D. Baran, I. McCulloch, *Chemical Society Reviews* **2019**, *48*, 1596-1625; d) P. Cheng, G. Li, X. Zhan, Y. Yang, *Nat. Photonics* **2018**, *12*, 131-142; e) W. Chen, Q. Zhang, *J. Mater. Chem. C* **2017**, *5*, 1275-1302; f) S. Li, W. Liu, C.-Z. Li, M. Shi, H. Chen, *Small* **2017**, *13*, 1701120.

[4] Y. Lin, J. Wang, Z.-G. Zhang, H. Bai, Y. Li, D. Zhu, X. Zhan, *Adv. Mater.* **2015**, *27*, 1170-1174.

[5] Y. Huang, E. J. Kramer, A. J. Heeger, G. C. Bazan, *Chem. Rev.* **2014**, *114*, 7006-7043.

[6] a) B. Sanchez-Lengeling, L. M. Roch, J. D. Perea, S. Langner, C. J. Brabec, A. Aspuru-Guzik, *Adv Theor Simul* **2019**, *2*; b) S. E. Root, S. Savagatrup, C. J. Pais, G. Arya, D. J. Lipomi, *Macromolecules* **2016**, *49*, 2886-2894; c) W. L. Zhang, E. D. Gomez, S. T. Milner, *Phys Rev Lett* **2017**, *119*; d) R. Alessandri, J. J. Uusitalo, A. H. de Vries, R. W. A. Havenith, S. J. Marrink, *J. Am. Chem. Soc.* **2017**, *139*, 3697-3705; e) J. M. Y. Carrillo, Z. Seibers, R. Kumar, M. A. Matheson, J. R. Ankner, M. Goswami, K. Bhaskaran-Nair, W. A. Shelton, B. G. Sumpter, S. M. Kilbey, *Acs Nano* **2016**, *10*, 7008-7022.

[7] a) A. O. Weldeab, A. Steen, D. J. Starkenburg, J. S. D. Williams, K. A. Abboud, J. Xue, N. I. Hammer, R. K. Castellano, D. L. Watkins, *J. Mater. Chem. C* **2018**, *6*, 11992-12000; b) G. Han, Y. Guo, X. Song, Y. Wang, Y. Yi, *J. Mater. Chem. C* **2017**, *5*, 4852-4857; c) R. Fitzner, C. Elschner, M. Weil, C. Uhrich, C. Körner, M. Riede, K. Leo, M. Pfeiffer, E. Reinold, E. Mena-Osteritz, P. Bäuerle, *Adv. Mater.* **2012**, *24*, 675-680; d) P. E. Hartnett, E. A. Margulies, H. S. S. R. Matte, M. C. Hersam, T. J. Marks, M. R. Wasielewski, *Chem. Mater.* **2016**, *28*, 3928-3936; e) P. E. Hartnett, A. Timalsina, H. S. S. R. Matte, N. Zhou, X. Guo, W. Zhao, A. Facchetti, R. P. H. Chang, M. C. Hersam, M. R. Wasielewski, T. J. Marks, *J. Am. Chem. Soc.* **2014**, *136*, 16345-16356.

[8] a) T. J. Aldrich, M. Matta, W. Zhu, S. M. Swick, C. L. Stern, G. C. Schatz, A. Facchetti, F. S. Melkonyan, T. J. Marks, *J. Am. Chem. Soc.* **2019**, *141*, 3274-3287; b) S. M. Swick, W. Zhu, M. Matta, T. J. Aldrich, A. Harbuzaru, J. T. Lopez Navarrete, R. Ponce Ortiz, K. L. Kohlstedt, G. C. Schatz, A. Facchetti, F. S. Melkonyan, T. J. Marks, *P. Natl. Acad. Sci. USA* **2018**, *115*, E8341-E8348.

[9] a) H. Zhang, H. Yao, J. Hou, J. Zhu, J. Zhang, W. Li, R. Yu, B. Gao, S. Zhang, J. Hou, *Adv. Mater.* **2018**, *30*, 1800613; b) Y. Lin, Q. He, F. Zhao, L. Huo, J. Mai, X. Lu, C.-J. Su, T. Li, J. Wang, J. Zhu, Y. Sun, C. Wang, X. Zhan, *J. Am. Chem. Soc.* **2016**, *138*, 2973-2976; c) X. Shi, L. Zuo, S. B. Jo, K. Gao, F. Lin, F. Liu, A. K. Y. Jen, *Chem. Mater.* **2017**, *29*, 8369-8376; d) Z. Liang, M. Li, X. Zhang, Q. Wang, Y. Jiang, H. Tian, Y. Geng, *J. Mater. Chem. A* **2018**, *6*, 8059-8067; e) X. Shi, X. Liao, K. Gao, L. Zuo, J. Chen, J. Zhao, F. Liu, Y. Chen, A. K.-Y. Jen, *Adv. Funct. Mater.* **2018**, *28*, 1802324; f) T. J. Aldrich, S. M. Swick, F. S. Melkonyan, T. J. Marks, *Chem. Mater.* **2017**, *29*, 10294-10298; g) Y.-C. Lin, Y.-J. Lu, C.-S. Tsao, A. Saeki, J.-X. Li, C.-H. Chen, H.-C. Wang, H.-C. Chen, D. Meng, K.-H. Wu, Y. Yang, K.-H. Wei, *J. Mater. Chem. A* **2019**, *7*, 3072-3082.

[10] D. Yan, W. Liu, J. Yao, C. Zhan, *Adv. Energy. Mater.* **2018**, *8*, 1800204.

[11] a) L. J. Wang, Q. K. Li, Z. G. Shuai, L. P. Chen, Q. Shi, *Phys. Chem. Chem. Phys.* **2010**, *12*, 3309-3314; b) A. S. Eggeman, S. Illig, A. Troisi, H. Sirringhaus, P. A. Midgley, *Nat. Mater.* **2013**, *12*, 1044-1048; c) B. M. Savoie, K. L. Kohlstedt, N. E. Jackson, L. X. Chen, M. O. de la Cruz, G. C. Schatz, T. J. Marks, M. A. Ratner, *P. Natl. Acad. Sci. USA* **2014**, *111*, 10055-10060; d) N. E. Jackson, K. L. Kohlstedt, L. X. Chen, M. A. Ratner, *J. Chem. Phys.* **2016**, *145*; e) K. M. Pelzer, A. Vazquez-Mayagoitia, L. E. Ratcliff, S. Tretiak, R. A. Bair, S. K. Gray, T. Van Voorhis, R. E. Larsen, S. B. Darling, *Chem Sci* **2017**, *8*, 2597-2609.

[12] H. Geng, Q. Peng, L. J. Wang, H. J. Li, Y. Liao, Z. Y. Ma, Z. G. Shuai, *Adv. Mater.* **2012**, *24*, 3568-3572.

[13] L. Ye, B. A. Collins, X. C. Jiao, J. B. Zhao, H. Yan, H. Ade, *Adv. Energy. Mater.* **2018**, *8*.

[14] a) A. A. Y. Guilbert, M. Zbiri, A. D. F. Dunbar, J. Nelson, *J. Phys. Chem. B.* **2017**, *121*, 9073-9080; b) W. C. Huang, N. Chandrasekaran, S. K. K. Prasad, E. Gann, L. Thomsen, D. Kabra, J. M. Hodgkiss, Y. B. Cheng, C. R. McNeill, *ACS Appl. Mater. Inter.* **2016**, *8*, 29608-29618; c) K. Vandewal, S. Himmelberger, A. Salleo, *Macromolecules* **2013**, *46*, 6379-6387; d) D. Gao, B. Djukic, W. Q. Shi, C. R. Bridges, L. M. Kozycz, D. S. Seferos, *ACS Appl. Mater. Inter.* **2013**, *5*, 8038-8043.

[15] N. E. Jackson, K. L. Kohlstedt, B. M. Savoie, M. O. de la Cruz, G. C. Schatz, L. X. Chen, M. A. Ratner, *J. Am. Chem. Soc.* **2015**, *137*, 6254-6262.

[16] a) N. D. Treat, A. Varotto, C. J. Takacs, N. Batara, M. Al-Hashimi, M. J. Heeney, A. J. Heeger, F. Wudl, C. J. Hawker, M. L. Chabinyc, *J. Am. Chem. Soc.* **2012**, *134*, 15869-15879; b) M. Ghasemi, H. W. Hu, Z. X. Peng, J. J. Rech, I. Angunawela, J. H. Carpenter, S. J. Stuard, A. Wadsworth, I. McCulloch, W. You, H. Ade, *Joule* **2019**, *3*, 1328-1348.

[17] a) A. G. Gagorik, B. Savoie, N. Jackson, A. Agrawal, A. Choudhary, M. A. Ratner, G. C. Schatz, K. L. Kohlstedt, *J. Phys. Chem. Lett.* **2017**, *8*, 415-421; b) N. E. Jackson, L. X. Chen, M. A. Ratner, *P. Natl. Acad. Sci. USA* **2016**, *113*, 8595-8600.

[18] a) E. Jankowski, H. S. Marsh, A. Jayaraman, *Macromolecules* **2013**, *46*, 5775-5785; b) S. E. Root, N. E. Jackson, S. Savagatrup, G. Arya, D. J. Lipomi, *Energ. Environ. Sci.* **2017**, *10*, 558-569.

[19] S. Gelinas, A. Rao, A. Kumar, S. L. Smith, A. W. Chin, J. Clark, T. S. van der Poll, G. C. Bazan, R. H. Friend, *Science* **2014**, *343*, 512-516.

[20] T. Liu, A. Troisi, *Adv. Mater.* **2013**, *25*, 1038-1041.

[21] a) M. Campoy-Quiles, T. Ferenczi, T. Agostinelli, P. G. Etchegoin, Y. Kim, T. D. Anthopoulos, P. N. Stavrinou, D. D. C. Bradley, J. Nelson, *Nat. Mater.* **2008**, *7*, 158-164; b) B. Watts, W. J. Belcher, L. Thomsen, H. Ade, P. C. Dastoor, *Macromolecules* **2009**, *42*, 8392-8397.

[22] D. L. Cheung, A. Troisi, *J. Phys. Chem. C.* **2010**, *114*, 20479-20488.

[23] a) J. Nelson, J. J. Kwiatkowski, J. Kirkpatrick, J. M. Frost, *Accounts Chem. Res.* **2009**, *42*, 1768-1778; b) N. R. Tummala, S. Mehraeen, Y. T. Fu, C. Risko, J. L. Bredas, *Adv. Funct. Mater.* **2013**, *23*, 5800-5813.

[24] A. Zhugayevych, S. Tretiak, *Annu. Rev. Phys. Chem.* **2015**, *66*, 305-+.

[25] a) R. C. I. MacKenzie, C. G. Shuttle, G. F. Dibb, N. Treat, E. von Hauff, M. J. Robb, C. J. Hawker, M. L. Chabinyc, J. Nelson, *J. Phys. Chem. C.* **2013**, *117*, 12407-12414; b) B. M. Savoie, A. Rao, A. A. Bakulin, S. Gelinas, B. Movaghar, R. H. Friend, T. J. Marks, M. A. Ratner, *J. Am. Chem. Soc.* **2014**, *136*, 2876-2884; c) H. Bassler, A. Kohler, *Unimolecular and Supramolecular Electronics I: Chemistry and Physics Meet at Metal-Molecule Interfaces* **2012**, *312*, 1-65.

[26] a) S. L. Smith, A. W. Chin, *Phys Rev B* **2015**, *91*; b) V. Zolyomi, J. Koltai, J. Kurti, S. Pekker, *Phys. Status Solidi B* **2008**, *245*, 2018-2021.

[27] J. D. Chai, M. Head-Gordon, *Phys. Chem. Chem. Phys.* **2008**, *10*, 6615-6620.

[28] a) H. Huang, L. Yang, A. Facchetti, T. J. Marks, *Chem. Rev.* **2017**, *117*, 10291-10318; b) J. Chen, Q. Liao, G. Wang, Z. Yan, H. Wang, Y. Wang, X. Zhang, Y. Tang, A. Facchetti, T. J. Marks, X. Guo, *Macromolecules* **2018**, *51*, 3874-3885; c) X. Guo, Q. Liao, E. F. Manley, Z. Wu, Y. Wang, W. Wang, T. Yang, Y.-E. Shin, X. Cheng, Y. Liang, L. X. Chen, K.-J. Baeg, T. J. Marks, X. Guo, *Chemistry of Materials* **2016**, *28*, 2449-2460.

[29] a) Y. Lin, F. Zhao, Q. He, L. Huo, Y. Wu, T. C. Parker, W. Ma, Y. Sun, C. Wang, D. Zhu, A. J. Heeger, S. R. Marder, X. Zhan, *J. Am. Chem. Soc.* **2016**, *138*, 4955-4961; b) W. Gao, Q. An, R. Ming, D. Xie, K. Wu, Z. Luo, Y. Zou, F. Zhang, C. Yang, *Adv. Funct. Mater.* **2017**, *27*, 1702194.

[30] a) Y. Yang, Z.-G. Zhang, H. Bin, S. Chen, L. Gao, L. Xue, C. Yang, Y. Li, *J. Am. Chem. Soc.* **2016**, *138*, 15011-15018; b) C. e. Zhang, S. Feng, Y. Liu, R. Hou, Z. Zhang, X. Xu, Y. Wu, Z. Bo, *ACS Appl. Mater. Inter.* **2017**, *9*, 33906-33912.

[31] a) F. Zhao, S. Dai, Y. Wu, Q. Zhang, J. Wang, L. Jiang, Q. Ling, Z. Wei, W. Ma, W. You, C. Wang, X. Zhan, *Adv. Mater.* **2017**, *29*, 1700144; b) J. Zhu, S. Li, X. Liu, H. Yao, F. Wang, S. Zhang, M. Sun, J. Hou, *J. Mater. Chem. A* **2017**, *5*, 15175-15182; c) S. Li, L. Ye, W. Zhao, S. Zhang, S. Mukherjee, H. Ade, J. Hou, *Adv. Mater.* **2016**, *28*, 9423-9429; d) Z. Zhang, L. Feng, S. Xu, J. Yuan, Z.-G. Zhang, H. Peng, Y. Li, Y. Zou, *J. Mater. Chem. A* **2017**, *5*, 11286-11293.

[32] a) F. Neese, *Wiley Interdisciplinary Reviews: Computational Molecular Science* **2012**, *2*, 73-78; b) K. James, *Int. J. Quantum Chem.* **2008**, *108*, 51-56.

[33] A. Kuzmich, D. Padula, H. B. Ma, A. Troisi, *Energ. Environ. Sci.* **2017**, *10*, 395-401.

[34] a) C. Zheng, C. Zhong, C. J. Collison, F. C. Spano, *J. Phys. Chem. C* **2019**, *123*, 3203-3215; b) D. Arundhati, K. Danielle, C. Chern, C. Danielle, C. Jianshu, C. Justin, **2019**.

[35] a) J. A. K. Howard, V. J. Hoy, D. O'Hagan, G. T. Smith, *Tetrahedron* **1996**, *52*, 12613-12622; b) J. D. Dunitz, R. Taylor, *Chemistry – A European Journal* **1997**, *3*, 89-98.

[36] a) E. F. Manley, J. Strzalka, T. J. Fauvell, N. E. Jackson, M. J. Leonardi, N. D. Eastham, T. J. Marks, L. X. Chen, *Adv Mater* **2017**, *29*, 1703933; b) E. F. Manley, J. Strzalka, T. J. Fauvell, T. J. Marks, L. X. Chen, *Adv Energy Mater* **2018**, *8*, 1800611.

[37] M. Williams, N. R. Tummala, S. G. Aziz, C. Risko, J.-L. Brédas, *J. Phys. Chem. Lett.* **2014**, *5*, 3427-3433.

[38] a) F. Gajdos, H. Oberhofer, M. Dupuis, J. Blumberger, *J. Phys. Chem. Lett.* **2013**, *4*, 1012-1017; b) F. Gajdos, H. Oberhofer, M. Dupuis, J. Blumberger, *J. Phys. Chem. Lett.* **2014**, *5*, 2765-2766.

[39] B. M. Savoie, K. L. Kohlstedt, N. E. Jackson, L. X. Chen, M. Olvera de la Cruz, G. C. Schatz, T. J. Marks, M. A. Ratner, *P. Natl. Acad. Sci. USA* **2014**, *111*, 10055-10060.

[40] a) M. C. R. Delgado, E.-G. Kim, D. A. d. S. Filho, J.-L. Bredas, *J. Am. Chem. Soc.* **2010**, *132*, 3375-3387; b) S. W. Eaton, L. E. Shoer, S. D. Karlen, S. M. Dyar, E. A. Margulies, B. S. Veldkamp, C. Ramanan, D. A. Hartzler, S. Savikhin, T. J. Marks, M. R. Wasielewski, *J. Am. Chem. Soc.* **2013**, *135*, 14701-14712.

[41] J. Vura-Weis, M. A. Ratner, M. R. Wasielewski, *J. Am. Chem. Soc.* **2010**, *132*, 1738-1739.

[42] a) Z. Liu, Y. Wu, Q. Zhang, X. Gao, *J. Mater. Chem. A* **2016**, *4*, 17604-17622; b) J. Wang, X. Zhan, *Trends in Chemistry* **2019**.

[43] a) J. Zhang, Y. Li, J. Huang, H. Hu, G. Zhang, T. Ma, P. C. Y. Chow, H. Ade, D. Pan, H. Yan, *J. Am. Chem. Soc.* **2017**, *139*, 16092-16095; b) Y. Zhong, B. Kumar, S. Oh, M. T. Trinh, Y. Wu, K. Elbert, P. Li, X. Zhu, S. Xiao, F. Ng, M. L. Steigerwald, C. Nuckolls, *J. Am. Chem. Soc.* **2014**, *136*, 8122-8130; c) K. Lin, S. Wang, Z. Wang, Q. Yin, X. Liu, J. Jia, X. e. Jia, P. Luo, X. Jiang, C. Duan, F. Huang, Y. Cao, *Frontiers in Chemistry* **2018**, *6*; d) D. Meng, H. Fu, C. Xiao, X. Meng, T. Winands, W. Ma, W. Wei, B. Fan, L. Huo, N. L. Doltsinis, Y. Li, Y. Sun, Z. Wang, *J. Am. Chem. Soc.* **2016**, *138*, 10184-10190.

[44] A. D. Hendsbee, J.-P. Sun, W. K. Law, H. Yan, I. G. Hill, D. M. Spasyuk, G. C. Welch, *Chem. Mater.* **2016**, *28*, 7098-7109.

ARTICLE

Crystal Structures and

Steven M. Swick, Tim Gebraad

Computations for Organic Solar Cells: Single crystal x-ray structures provide atomistic details of molecular packing in the solid state, but has been underutilized in the organic photovoltaic community. Here, we correlate the structure of **ITIC** derivatives to crystal structure and electronic/charge transporting properties computationally derived from the structures.

Leighton Jones, Bo Fu, Thomas J. Aldrich, Kevin L. Kohlstedt, George C. Schatz*, Antonio Facchetti*, Tobin J. Marks**

Page No. – Page No.

Building Blocks for High-Efficiency Organic Photovoltaics. Interplay of Molecular, Crystal, and Electronic Properties of Post-Fullerene ITIC Ensembles